

A global view of the stratospheric background, volcanic and wildfire aerosol in the CALIOP era (2006 – 2023)

Bengt G. Martinsson, Johan Friberg, and Moa K. Sporre

Department of Physics, Lund University, Lund, Sweden

Correspondence to: Bengt G. Martinsson (bengt.martinsson@fysik.lu.se)

Abstract. This study deals with the stratospheric aerosol during the 17 years of lidar measurements with CALIOP [aboard the CALIPSO satellite](#). To obtain extinction from the backscattering measurements, we estimated the lidar ratios of the main aerosol injections into the stratosphere. The stratospheric background is estimated by making a subdivision of the stratosphere into nine parts, spanned by three latitude and altitude intervals, reaching background conditions individually at different times. The extracted background shows excellent agreement with [SAGE II](#) solar occultation measurements in the volcanically quiescent period 1998 - 2000. Our results show that 70% of the background aerosol in the deep Brewer-Dobson (dBD) branch is formed above 19 km altitude, indicating strong influence of carbonyl sulfide on the stratospheric background aerosol. The stratosphere was clearly affected by 15 volcanic eruptions and 5 wildfires. Their combined aerosol load affected [the](#) Southern extratropics, tropics and Northern extratropics almost equally, and the altitude distribution shows that the shallow Brewer-Dobson branch was most affected (43%) followed by the dBD (31%) and lowermost stratosphere (26%). The most important events in order of maximum AOD were the Hunga Ha'apai eruption (2022), Australian wildfires (2019-20) and the eruptions of Raikoke (2019), Sarychev (2009) and Nabro (2011). These events induced strong variability in the [yearly average global](#) stratospheric aerosol optical depth (AOD), [which ranged from 0.0057 \(background\) to 0.016. causing highly variable climate impact in the period studied with yearly average global effective radiative forcing ranging from -0.14 W/m² at background conditions to -0.4 W/m².](#) CALIOP provided [important invaluable](#) data for stratospheric aerosol climatologies during its 17 years of operation.

28

29 **1. Introduction**

30 Tropospheric air, containing aerosol particles and the sulfurous aerosol precursor gases
31 carbonyl sulfide (OCS) and sulfur dioxide (SO₂), enter the stratosphere across the
32 tropical tropopause. These constituents form the stratospheric background aerosol
33 (Kremser et al., 2016), an aerosol layer that is located above 20 km altitude in the
34 tropics, and lower in the extratropics, containing water-soluble sulfur-rich particles
35 (Junge et al., 1961). Additional aerosol, that can be classified as background due to its
36 diffuse nature, originates from the Asian Tropopause Aerosol Layer (ATAL), an aerosol
37 layer between 13 – 18 km altitude over Asia (Vernier et al., 2015). The stratospheric
38 background aerosol contains sulfate, water, organics, and minor traces of tropospheric
39 aerosol and extraterrestrial material (Martinsson et al., 2005; Murphy et al., 2007;
40 Kremser et al., 2016; Martinsson et al., 2019).

41 The stratospheric aerosol load is highly variable due to special aerosol events
42 connected to volcanism (Bauman et al., 2003; Vernier et al., 2009; Solomon et al., 2011;
43 Andersson et al., 2015) and wildfires (Fromm et al., 2010; Martinsson et al., 2022;
44 Friberg et al., 2023, Peterson et al., 2025), which inject copious amounts of aerosol and
45 precursor gases affecting the stratospheric aerosol for months up to several years
46 (Friberg et al., 2018). These aerosol events induce a variability that needs to be
47 accounted for in climate models. From 1979, the satellite measurement era, the most
48 important volcanic eruptions, El Chichon in 1982 and Mt. Pinatubo (1991), caused a
49 maximum global 3-month average effective radiative forcing of -2 and -3 W/m²,
50 respectively (Schmidt et al., 2018). After a period of low volcanic influence on the
51 stratosphere around the turn of the millennium, many volcanic eruptions and wildfires
52 have affected the aerosol in the stratosphere. The most important are the 2019-20
53 Australian wildfires and the eruptions of Sarychev (2009), Raikoke (2019) and Hunga
54 Ha’apai (2022).

55 Fresh wildfire aerosol particles contain black carbon and a dominating fraction of
56 organics (Garofalo et al., 2019), where the latter is rapidly lost (half-life 10 days) in the
57 stratosphere due to photolysis (Martinsson et al., 2022). The composition of volcanic
58 stratospheric aerosol particles varies. SO₂-rich volcanic emissions, like the 2008

59 eruption of Kasatochi, are dominated by sulfate, some organics and a minor fraction of
60 ash (Martinsson et al., 2009, Andersson et al., 2013; Friberg et al., 2014). On the other
61 hand, SO₂-poor eruptions, like that of Puyehue-Cordón Caulle in 2011, are dominated
62 by ash (Clarisse et al., 2013). Steam-boosted eruptions of submarine volcanoes (Mastin
63 et al., 2024), like the 2022 eruption of Hunga Ha’apai, can result in a stratospheric
64 aerosol with a strong contribution from sea salt (Martinsson et al., 2025).

65 From the beginning of extensive satellite data in the late 1970s the stratospheric aerosol
66 load has usually been measured using solar occultation (Sato et al., 1993). GloSSAC
67 (Global Space-based Stratospheric Aerosol Climatology), a later construction of a
68 continuous record of optical properties of stratospheric aerosol spanning 1979 to
69 present, has a core of solar occultation measurement with the notable 22 year era of
70 SAGE II continuing a few years of solar occultation measurement by SAM II and SAGE I
71 (Thomason et al., 2018). Solar occultation became unavailable during 2005 – 2017. To
72 continue the GloSSAC record, other satellite-based measurements were deployed. The
73 limb scatter instrument OSIRIS (Rieger et al., 2015) and the lidar CALIOP (Cloud-Aerosol
74 Lidar with Orthogonal Polarization) (Winker et al., 2010) were, after substantial
75 recalibration (Thomason et al., 2018, Kovilakam et al., 2020, Kovilakam et al., 2023),
76 used to bridge the gap to obtain continuous time series of stratospheric aerosol
77 properties. Mixing data from many sources that are relying on different measurement
78 principles is however complex, as pointed out by Thomason et al. (2018). We will
79 ~~discuss return to~~ this matter ~~further~~ in ~~the discussion~~ section 4.4.

80 This work deals with the stratospheric aerosol in the CALIOP era, spanning the 17-year
81 period 2006-06-12 to 2023-06-30. CALIOP data (level 1B, version 4-51) is corrected for
82 attenuation, and the lidar ratio is estimated for the stratospheric aerosol resulting from
83 12 volcanic eruptions and wildfires. The stratosphere from the tropopause to 35 km
84 altitude is divided into three altitude and three latitude parts, in total nine parts, where
85 the backscattering of the background stratospheric aerosol is identified and its sources
86 discussed. By subtraction of the signal from the background aerosol, the backscattering
87 from major stratospheric aerosol events is obtained. This is converted to AOD using the
88 estimated lidar ratios. We find that global average aerosol backscattering ~~intensity~~
89 ~~onintensity~~ exceeded the background by 55% in the 17 years studied. The strongest

90 influence from volcanism and wildfires was in 2022 and 2023 due to the submarine
91 Hunga Ha'apai eruption. The second strongest occurred in 2020 due to the Australian
92 wildfires, followed by 2009 (Sarychev eruption) and 2019 (mainly the Raikoke eruption).
93 2013 was a year when the entire stratosphere was close to background conditions.
94 Finally, we discuss the validity of lidar data in comparison with the more established
95 data based on solar occultation.

96 **2. Methods**

97 This paper is based on measurements with the CALIOP lidar instrument aboard the
98 CALIPSO (Cloud-Aerosol Lidar and Infrared Pathfinder Satellite Observation) satellite
99 that completed approximately 15 orbits between latitudes -82 and 82° each day.

100 ***2.1 CALIOP properties and methods applied***

101 CALIOP with a laser of 532 nm wavelength produced vertical profiles of backscattering
102 intensity from air molecules, aerosol particles and cloud drops from the ground up to 35
103 km altitude with high vertical resolution depending on altitude. In the altitude ranges <
104 8.2, 8.2 - 20.2, 20.2 – 30.1 and >30.1 km the vertical resolution is 30, 60, 180 and 300 m,
105 respectively (Winker et al., 2007, 2010). Here we use data only from the stratosphere,
106 where the tropopause altitude according to MERRA-2 reanalysis (Modern-Era
107 Retrospective analysis for Research and Applications) (Gelaro et al., 2017) was used to
108 discriminate data from the troposphere. Only data recorded during nighttime were used
109 in the general evaluation concerning all the CALIOP data available (Friberg et al., 2018;
110 Martinsson et al., 2022), implying that data will be missing at high latitudes for part of
111 the year with the strongest influence at the summer solstice. Data are also missing at
112 high latitudes mainly in the southern hemisphere due to influence from polar
113 stratospheric clouds. The data were extrapolated linearly to cover all the way to 80°
114 latitude in both hemispheres. ~~The uncertainties in~~ the global perspective used here ~~are~~
115 ~~minor due to the small~~ the fraction of the earth's surface area ~~of the earth~~ affected by
116 the extrapolation is 8.7% at the summer solstice and 3.5% two months before/after that
117 time. In most cases the quantitative impact on the global AOD is small, but in special
118 cases, like the eruption of the Icelandic volcano Grimsvötn (64° N) on 21 May 2011, the

119 [inability to measure at high latitudes causes larger quantitative errors \(Andersson et al.,](#)
120 [2015\).](#)

121 The evaluation is based on version 4-51 of CALIOP level 1B data (NASA/LARC/SD/ASDC,
122 2024). Clouds within 3km above the tropopause were discriminated based on
123 depolarization of the signal obtained from the CALIOP instrument, polar stratospheric
124 clouds were discriminated based on temperature and data taken in the South Atlantic
125 Anomaly are filtered out as explained in Friberg et al. (2018) and Martinsson et al.
126 (2022). The backscatter data were corrected for attenuation by methodology described
127 in Martinsson et al. (2022) and were first converted to extinction by the standard
128 effective lidar ratio $S = 50$ sr used for CALIOP (Kar et al., 2019). Volcanic eruptions and
129 wildfires with lidar ratio deviating from 50 sr by more than 5% were corrected, see
130 sections 2.3 and [4.23.4](#).

131 The stratospheric CALIOP level 3 product (Kar et al., 2019) and the data presented here
132 are both based on the CALIOP level 1B data set but differ with respect to latitude-,
133 longitude- and time-resolution, where CALIOP level 3 is based on monthly averages and
134 we normally use a time-resolution of 1 – 8 days depending on issue investigated. These
135 data sets also differ ~~in~~ with respect to lidar ratios: CALIOP level 3 extinction is obtained
136 based on a fixed lidar ratio of 50 sr, whereas we, when possible, estimate effective lidar
137 ratios for aerosol from individual volcanic eruptions and wildfires as described in
138 sections 2.3, 3.1 and [4.23.4](#). The notion “effective” relates to that CALIOP is affected by
139 multiple scattering, implying that use of lidar ratios for measurements unaffected by
140 multiple scattering, i.e., the true physical relation between extinction and
141 backscattering of the aerosol studied, will result in overestimation the extinction (Prata
142 et al., 2017; Martinsson et al., 2022). Another difference between CALIOP level 3 and
143 our method is that we correct data for attenuation of the detected scattered light
144 (Martinsson et al., 2022), which is important for identification and quantification of
145 aerosol processes in wildfire aerosol (Martinsson et al., 2022; Friberg et al., 2023) and
146 volcanic aerosol (Martinsson et al., 2025) and to obtain the AOD without influence from
147 attenuation.

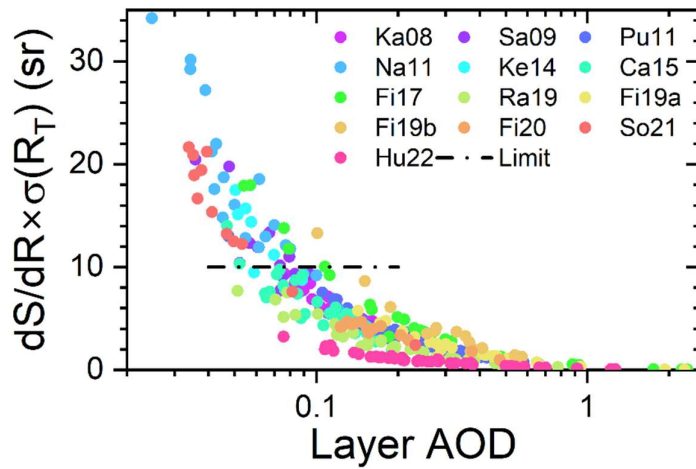
148 **2.2 Estimation of the stratospheric background**

149 The stratospheric aerosol background can rarely be observed in the entire stratosphere.
150 The last time the stratosphere was practically unaffected by injections from volcanic
151 eruptions and wildfires for several years was a few years around the turn of the
152 millennium (Solomon et al., 2011). Still, we need to find means to estimate the
153 stratospheric background because we can estimate the lidar ratio of stratospheric
154 injections from volcanic eruptions and wildfires (presented in next section) but not for
155 the background aerosol. Injections from aerosol events seldom affect the entire
156 stratosphere. Therefore, parts of the stratosphere can be in background conditions
157 when other parts are affected by aerosol injections.

158 To study the background conditions, the stratosphere was subdivided into nine parts
159 spanned by three altitude layers: the lowermost stratosphere (LMS, from the
160 tropopause to the 380 K isentrope, where the latter was obtained from MERRA-2
161 pressures and temperatures), the shallow Brewer-Dobson branch (sBD, between
162 isentropes 380 and 470 K) and the deep Brewer-Dobson branch (dBD, from the 470 K
163 isentrope to 35 km altitude), and three latitude regions: the Southern extratropics
164 (latitudes -80 to -20°), the tropics (latitudes -20 to 20°) and the Northern extratropics
165 (latitudes 20 to 80°)., Data were averaged over 8 days resulting in 46 observations per
166 year in each of the nine stratospheric parts. To estimate the background conditions in
167 this 17-year study, the averages of the three years with the lowest average
168 backscattering of each 8-day period were formed. For two of the nine stratospheric
169 parts, the tropical sBD and dBD, background conditions were rare, wherefore only the
170 two lowest years were used in these two stratospheric parts. The method applied
171 results in the minimum ~~concentration-aerosol load~~ observed during the 17-year period.
172 This means that in addition to the tropospheric aerosol and precursor gases entering
173 the stratosphere across the tropical tropopause in the large-scale stratospheric
174 circulation, phenomena such as the ATAL (Vernier et al., 2015) and other exchanges
175 across the extratropical tropopause are included in the background.

176 The extracted lowest 8-day values formed a seasonal pattern that was fitted by the sum
177 of a constant and a sinusoidal function. These fits were used to express the average
178 backscattering of the background aerosol in each of the nine stratospheric parts over
179 the 17 years spanned by CALIOP measurements. The average backscattering converts

180 to AOD when multiplied with the lidar ratio. The fitted background was subtracted from
 181 the measured total backscattering to form the backscattering from volcanic eruptions
 182 and wildfires. These background-subtracted average backscattering data were
 183 converted to AOD via the lidar ratios obtained from individual aerosol events, as
 184 described in the next section.



185

186 **Figure 1.** Relation between the layer AOD and the measure on the uncertainty of the
 187 lidar ratio estimation. dS/dR is the sensitivity of the lidar ratio (S) to small shifts of the
 188 target scattering ratio (R) and $\sigma(R_T)$ is the standard deviation of the target R of each
 189 eruption or wildfire obtained horizontally beside each aerosol layer investigated. Layers
 190 with uncertainty exceeding 10 sr (“limit”) are discarded in the following analysis.

191 **2.3 Lidar ratio**

192 The lidar ratio of the aerosol from the strongest volcanic eruptions and wildfires in the
 193 period studied was estimated based on methodology described in Martinsson et al.
 194 (2022), where individual dense aerosol layers are investigated. In that method a target
 195 value in scattering ratio (R) obtained horizontally beside the studied aerosol layer (R_T) is
 196 reached below the layer in an iterative procedure that results in an estimate of the
 197 effective lidar ratio, while correcting for attenuation of the backscattered signal. The
 198 effective lidar ratio obtained describes the average conditions of the entire layer where
 199 the optical properties in principle can vary. However, the lidar ratio estimates are
 200 obtained in dense aerosol layers, where the influence from background aerosol is small.

201 The uncertainty in the estimated lidar ratio depends on the AOD of the layer. A small
202 change in the lidar ratio (S) results in a substantial change in the scattering ratio (R)
203 below a dense layer, i.e., dS/dR is small for dense aerosol layers. dS/dR is obtained by
204 shifting R slightly around R_T . There is also an uncertainty in how well R_T represents the
205 aerosol beneath the layer. We estimate that uncertainty by the standard deviation of the
206 scattering ratio ($\sigma(R_T)$) obtained horizontally beside all the aerosol layers studied for
207 each volcanic eruption or wildfire. This is thus based on the assumption that the aerosol
208 horizontally beside and below the aerosol layer have the same standard deviation in R ,
209 but the actual scattering ratios horizontally beside and below an individual layer are
210 uncorrelated. The estimated uncertainty becomes $dS/dR \times \sigma(R_T)$. Figure 1 shows all
211 $dS/dR \times \sigma(R_T)$ related to the AOD of all the estimations of the lidar ratio. The uncertainty in
212 the lidar ratio estimate increases as the layer AOD decreases, hence a limit was set to
213 $dS/dR \times \sigma(R_T) < 10$ sr to pass as a lidar ratio estimate. As a result, most estimates for
214 three volcanic eruptions, 2011 Nabro (Na11), 2014 Kelut (Ke14), and 2021 Soufriere
215 (So21), among the 12 eruptions and wildfires analyzed were lost, as illustrated in Figure
216 1.

217 For simplicity all the CALIOP data were evaluated using the standard lidar ratio of $S_0 =$
218 50 sr in the general evaluation. In the study of individual aerosol layers (Figure 1) both
219 the AOD based on the estimated lidar ratio and that based on S_0 were computed, where
220 the latter (AOD_{50}) was used to obtain the deviation caused by using S_0 . This deviation
221 depends on the S/S_0 ratio and AOD_{50} , where the effect of S/S_0 is the dominant one
222 except for very dense aerosol layers. The result from the general evaluation is corrected
223 afterwards based on the [difference between ratio of \$S_0\$ and the estimated \$S\$](#) , see section
224 [4.23.4](#).

225 **3. Results**

226 Here we will present the stratospheric aerosol from the troposphere to 35 km altitude
227 and the latitude range -80 to 80° in the era of lidar measurements by the CALIOP
228 instrument aboard the CALIPSO satellite. CALIOP measured the backscattered intensity
229 from a 532 nm laser beam, which can be converted to extinction by multiplying with the
230 ratio of extinction to backscatter, i.e. the lidar ratio. Knowing the lidar ratio thus is

231 central for quantification by obtaining AOD from CALIOP measurements. We developed
 232 methodology to estimate the effective lidar ratio from CALIOP measurements, a
 233 methodology that also corrects for attenuation of the laser signal (Martinsson et al.,
 234 2022). Here we start by presenting the lidar ratio of the main aerosol events of the
 235 CALIOP era before giving an overview of the AOD in the period studied. Then we
 236 investigate separation of aerosol signals of aerosol events due to volcanic eruptions and
 237 wildfires from signals due to stratospheric background aerosol. This is followed by
 238 sections on corrections of AOD due to lidar ratio deviations from the commonly
 239 assumed 50 sr. Then we an overview overview of the AOD and a simplified estimate of
 240 the stratospheric aerosol's climate radiative impact.

241 **3.1 Lidar ratio**

242 The main aerosol events affecting the stratosphere in the CALIOP era are presented in
 243 Table 1. The methodology we use to estimate lidar ratios requires sufficiently dense
 244 aerosol layers as described in section 2, implying that some of the events mentioned in
 245 Table 1 are not suitable for the methodology. The lidar ratio was investigated for

246 **Table 1.** Major volcanic eruptions and wildfires affecting the stratospheric aerosol in the
 247 CALIOP era.

	Date	Volcano/wildfire	Lat ^a	Lon ^b	SO ₂ (Tg)	References
<i>Volcanic eruptions</i>						
1	2006-05-20	Soufriere Hills (Su)	17°	-62.2°	0.2	Carn and Prata (2010)
2	2006-10-07	Rabaul (Rb)	-4°	152°	0.23	Carn et al. (2009)
3	2008-08-07	Kasatochi (Ka)	52°	-176°	1.7	Thomas et al. (2011)
4	2009-06-12	Sarychev (Sa)	48°	153°	1.2	Haywood et al. (2010)
5	2010-10-05	Merapi (Me)	-7°	110°	0.44	Surono et al. (2012)
6	2011-06-05	Puyehue-Cordón Caulle (Pu)	-40°	-72°	0.25	Clarisse et al. (2012)
7	2011-06-12	Nabro (Na)	13°	42°	1.5	Clarisse et al. (2012)
8	2014-02-13	Kelut (Ke)	-8°	112°	0.18	Li et al. (2017)
9	2015-04-23	Calbuco (Ca)	-41°	-73°	0.3	Pardini et al. (2018)
10	2018-07-27	Ambae (Am)	-15°	168°	0.36	Malinina et al. (2021)
11	2019-06-22	Raikoke (Ra)	48°	153°	1.5	Kloss et al. (2021)
12	2019-06-26	Ulawun (Ul)	-5°	151°	0.14	Kloss et al. (2021)
13	2019-08-03	Ulawun (Ul)	-5°	151°	0.3	Kloss et al. (2021)
14	2021-04-10	Soufriere (So)	13°	-61°	0.31	Taylor et al. (2023)
15	2022-01-15	Hunga Ha'apai (Hu)	-21°	175°	0.45	Carn et al. (2022)

Wildfires

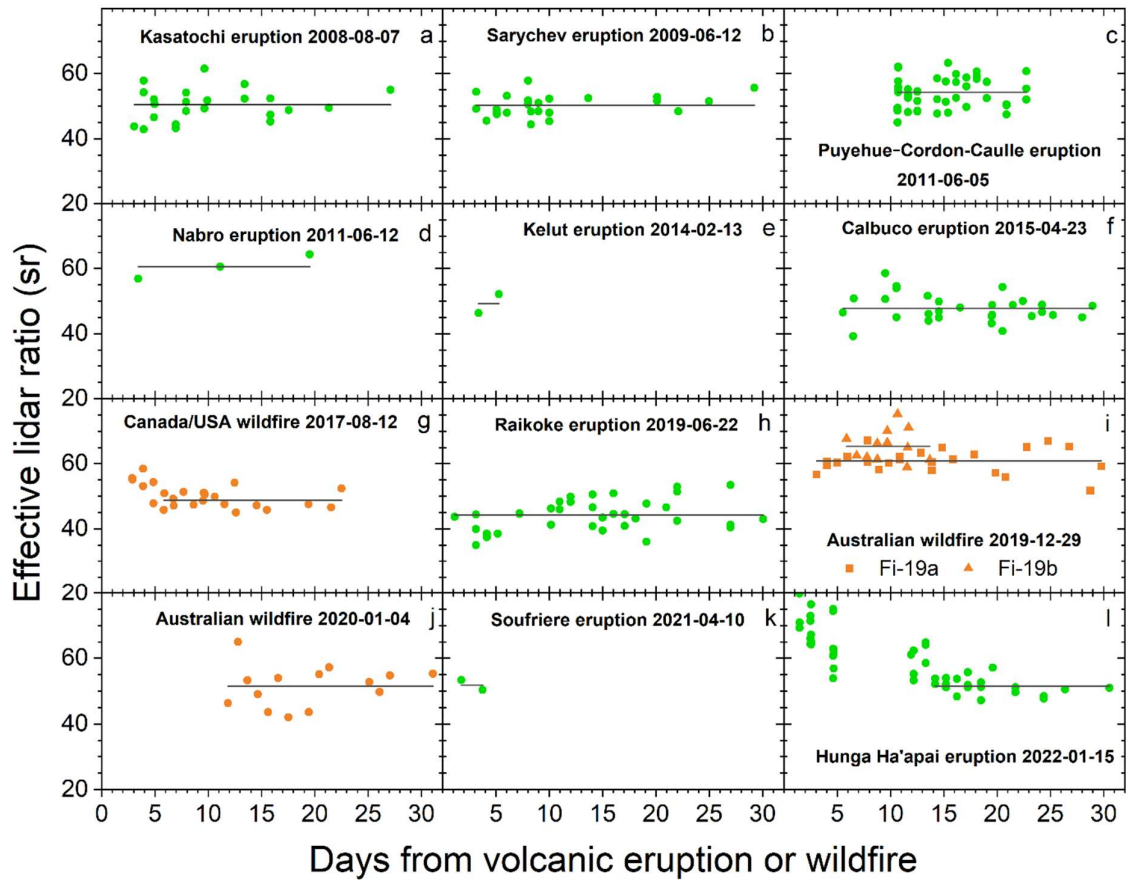
16	2006-12-19	Australia (A1)	-37°	147°	-	McCarthy et al. (2012)
17	2009-02-07	Australia (A2)	-38°	146°	-	Cruz et al. (2012)
18	2017-08-12	Canada/USA (CU)	53°	-123°	-	Fromm et al. (2021)
19	2019-12-29	Australia (A3)	-37°	149°	-	Peterson et al. (2021)
20	2020-01-04	Australia (A4)	-37°	149°	-	Peterson et al. (2021)

248

249 stratospheric aerosol from nine volcanic eruptions and three wildfire events (Figure 2).
 250 For some of these aerosol events the screening related to the uncertainty in the
 251 estimated lidar ratio (Figure 1) resulted in few observations, namely for the 2011 Nabro,
 252 2014 Kelut and the 2021 Soufriere eruptions. Most of the eruptions and wildfires display
 253 a stable lidar ratio during the first month, whereas two of the events show an initial
 254 decrease of the lidar ratio, the 2017 North American wildfire (Figure 2g) and the 2022
 255 Hunga Ha'apai eruption (Figure 2l), towards a stable value.

256 Effective lidar ratios are presented here which are best suited for application to
 257 measurements that, like CALIOP, are affected by multiple scattering (Martinsson et al.,
 258 2022). Compared with previous estimates, the results presented here are approximately
 259 20% lower than those of Prata et al. (2017) for the Kasatochi, Sarychev and Puyehue-
 260 Cordon Caulle eruptions, who estimated lidar ratio for measurements that are not
 261 affected by multiple scattering. Ohneiser et al. (2020) present Raman lidar measurements of
 262 the 2019 Australian wildfire (Table 1) that are not affected by multiple scattering. On 2020-01-09
 263 around 04:00 UTC (longitude -70.9, latitude -53.2) $S = 76$ sr was obtained. The closest CALIOP
 264 measurement in space and time that we evaluated was taken on the same day at 04:05,
 265 position (-43.4, -53.1) with $S = 75$ sr. The day before, at position (-57.2, -50.0) $S = 70$ sr and the
 266 day after at position (-55.0, -57.1) $S = 71$ sr. All these three measurements belong to the fires
 267 taking place last days of 2019, category B (outside the vortex) and are the three highest effective
 268 lidar ratios obtained in this category.

269 Stratospheric aerosol resulting from most volcanic eruptions and wildfires have a lidar
 270 ratio close to 50 sr, which is the commonly used lidar ratio for CALIOP data (Kar et al.,
 271 2019). Notable exceptions with lidar ratio deviating by more than 5% from 50 sr are the
 272 ash-dominated 2011 eruption of Puyehue-Cordón Caulle (Figure 2c), the 2019



273

274 **Figure 2.** Effective particle lidar ratios the first 30 days after a volcanic eruption or
 275 wildfire with a line displaying the average of each event. All measurements concurring
 276 with the condition $dS/dR \times \sigma(R) < 10$ are displayed for a) Kasatochi eruption 2008-08-07,
 277 b) Sarychev eruption 2009-06-12, c) Puyehue-Cordón-Caulle eruption 2011-06-05, d)
 278 Nabro eruption 2011-06-12, e) Kelut eruption 2014-02-13, f) Calbuco eruption 2015-04-
 279 23, g) Canada/USA wildfire 2017-08-12, h) Raikoke eruption 2019-06-22, i) Australian
 280 wildfire, 2019-12-29 subdivided in part Fi-19a (observations in the vortex (Kablik et al.,
 281 2020)) and Fi-19b (observations outside the vortex), j) Australian wildfire 2020-01-04, k)
 282 Soufriere eruption 2021-04-10 and l) Hunga Ha'apai eruption 2022-01-15. The averages
 283 include all data points except for the Canada/USA wildfire and the Hunga Ha'apai
 284 eruption where the initial decline in the lidar ratio is not part of the average represented
 285 by horizontal lines.

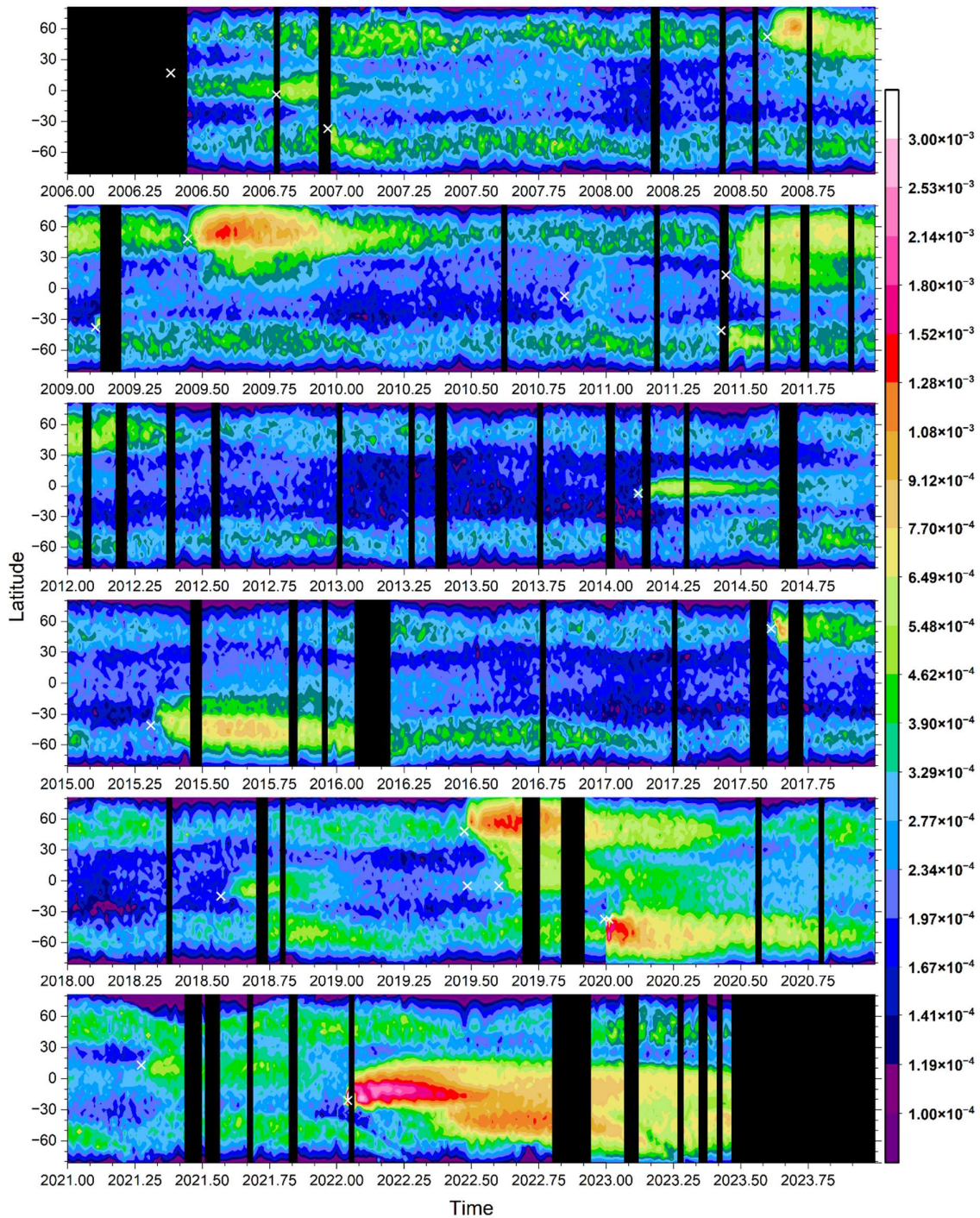
286

287 Raikoke eruption (Figure 2h) and the Australian wildfire in the last days of 2019 (Figure
288 2i). Also, the 2011 Nabro eruption (Figure 2d) tends to deviate from the commonly
289 adopted lidar ratio of 50 sr of stratospheric aerosol, however the observations are too
290 few for a firm conclusion. In the forthcoming presentation the lidar ratio of 50 sr will be
291 used before ~~a discussion on~~ the influence from deviations is addressed in sections
292 [4.23.4](#) and [4.33.5](#).

293 **3.2 Stratospheric aerosol events overview**

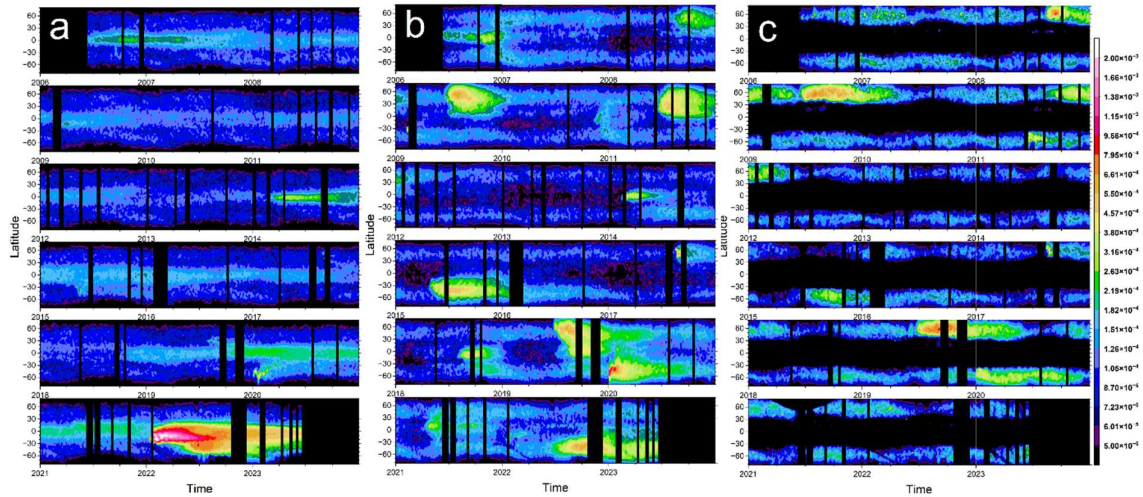
294 At least 15 volcanic eruptions and 5 wildfires clearly affected the stratospheric aerosol
295 in the CALIOP era (Table 1). The latitude distribution of the stratospheric aerosol from
296 the tropopause to 35 km altitude is shown in Figure 3, and subdivided into three layers,
297 dBD, sBD, and LMS, in [Figure 4 with full size versions in supplementary](#) Figures S1 – S3.
298 Additionally, the altitude distribution is shown in three latitude ranges [\(-80 to -20°, -20 to](#)
299 [20° and 20 to 80°\)](#) in [Figure 5 \(supplementary](#) Figures S4 – S6).

300 The influence from injections of aerosol from volcanic eruptions and wildfires has
301 durations of a few months to several years (Friberg et al., 2018). The latter category is
302 the aerosol events that enter the dBD branch in the tropics. The outstanding event
303 fulfilling this requirement in the period studied is the submarine eruption of Hunga
304 Ha’apai in 2022 (Figures [S1-4a](#) and [S55a, b](#)) where intense volcanism – sea interaction
305 (Seabrook et al., 2023; Mastin et al., 2024) formed large quantities of stratospheric
306 aerosol, ~~whereas aerosol formation from SO₂ could explain only ~30% of the AOD~~
307 (Martinsson et al., 2025). The remaining aerosol events in the dBD have much lower
308 AODs. The Kelut eruption in 2014 affected the dBD for approximately 4 years, ~~the. The~~
309 combined effect of the 2006 eruptions of Soufriere Hills and Rabaul (Figure [S55b](#)) show
310 similar long-term effects on the dBD in the tropics (Figure [S14a](#)). The combined effects
311 of 4 volcanic eruptions, the 2018 Ambae, the two 2019 Ulawun and the 2021 Soufriere
312 eruptions, gradually increased the dBD aerosol ~~concentration-load~~ in the tropics. In
313 addition to these tropical eruptions, some extratropical aerosol events affected the
314 dBD: the 2015 Calbuco eruption and some ~~overshooting~~ plumes ~~reaching injected~~
315 above the main ~~effluents-aerosol layer~~ of the 2019 Raikoke eruption. Three wildfires also
316 contributed aerosol to the extratropical dBD, the 2009 Australian, the 2017 Canada/USA
317 and the 2019 Australian wildfires. The aerosol from the latter fire formed a vortex where



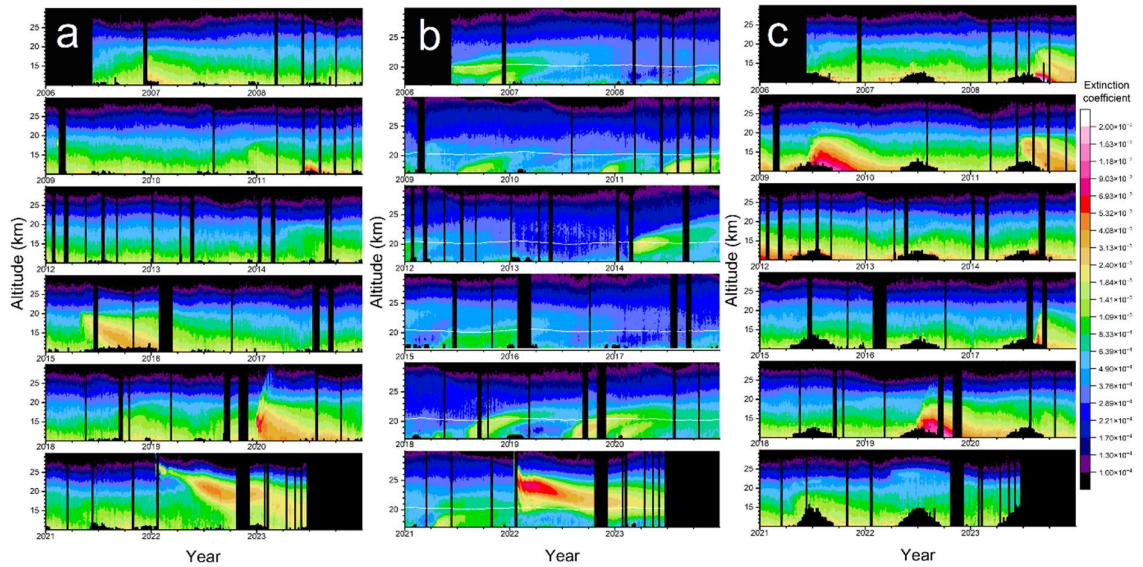
318

319 **Figure 3.** AOD integrated from the tropopause to 35 km altitude averaged over 4 days
 320 and 3 degrees in latitude. The lidar ratio is set to 50 sr. Color scale: The data is latitude
 321 weighted in the way that the Gglobal AOD contribution per degree of latitude is shown,
 322 i.e. the sum over latitude is the total AOD at any given time. The data has been
 323 extrapolated at high latitudes as described in section 2.1, Figure S7 shows the data
 324 without extrapolation. White crosses indicate time and latitude of aerosol events
 325 mentioned in Table 1.



326

327 [Figure 4. AOD integrated in three layers: a\) dBD, b\) sBD and c\) LMS. The color scale is](#)
 328 [latitude weighted as explained in the caption of Figure 3. Full size images are displayed](#)
 329 [in the Supplementary material, Figures S1 – S3.](#)



330

331 [Figure 5. Extinction coefficients \(\$\text{km}^{-1}\$ \) averaged in three latitude bands: a\) southern](#)
 332 [extratropics \(\$-80\$ to \$-20^\circ\$ \), b\) tropics \(\$-20\$ to \$20^\circ\$ \) and c\) northern extratropics \(\$20\$ to \$80^\circ\$ \).](#)
 333 [Full size images are displayed in the Supplementary material, Figures S4 – S6.](#)

334

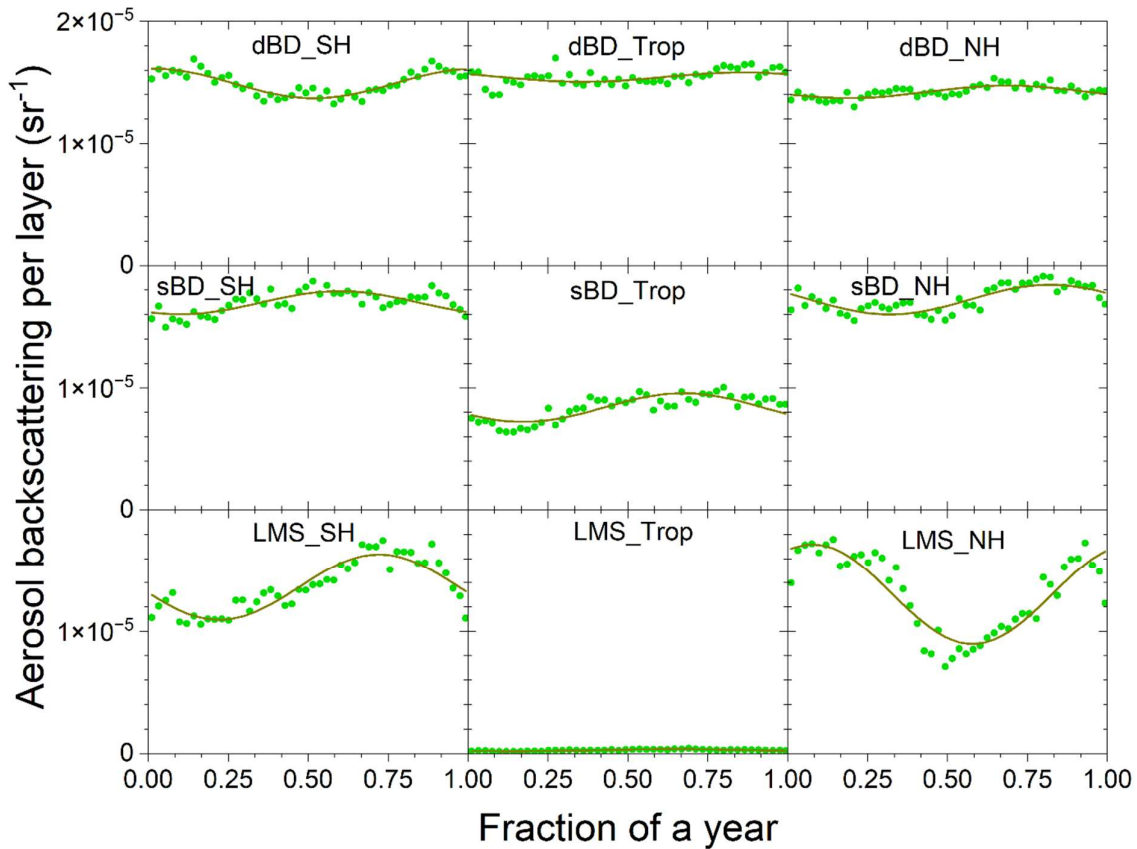
335 the aerosol rose above 31 km altitude (Kablick et al., 2020). The extratropical aerosol
336 events leave the dBD faster than the tropical ones because of the extratropical
337 downward motion of the BD circulation.

338 The shallow Brewer-Dobson (sBD) branch (Figure 4b) displays no such strong aerosol
339 event as the effect of the 2022 Hunga Ha’apai eruption on the dBD (Figure S24a). On the
340 other hand, many events had intermediate or small impacts. The Australian wildfires at
341 the end of 2019 and the beginning of 2020 made an initial strong impact that ~~was rapidly~~
342 ~~reduced by loss of (half-life 10 days) lost~~ 90% of the aerosol ~~with a half-life of 10 days,~~
343 likely due to photolysis of organic aerosol (Friberg et al., 2023), as did the 2017 North
344 American wildfire but with a lower aerosol load (Martinsson et al. 2022) and, to a still
345 lower extent, the 2009 Australian wildfire. The main volcanic eruptions affecting the sBD
346 branch were the 2008 Kasatochi, 2009 Sarychev, 2011 Nabro, 2015 Calbuco, 2019
347 Raikoke and, after a delay due to transport from the dBD branch, the 2022 Hunga
348 Ha’apai eruptions (Figure 4a, b). Other volcanos with smaller impact on the sBD branch
349 were the 2006 Soufriere Hills and Rabaul, the 2010 Merapi, 2014 Kelut, 2018 Ambae,
350 2019 Ulawun (2 eruptions) and 2021 Soufriere eruptions.

351 The LMS (Figure 4c), the last ~~passage-stratospheric part for passed by the~~ air and its
352 trace substances in the large-scale stratospheric circulation before exiting to the
353 troposphere, is affected by all stratospheric aerosol events. In addition, some
354 extratropical aerosol events do not reach beyond the LMS. The Kasatochi eruption
355 resulted in two distinct aerosol layers, a thin layer in the sBD whereas the main part of
356 its effluents was injected both sides of and close to the tropopause (Andersson et al.,
357 2015). Other exclusive LMS events in the period studied here are the 2011 Puyehue-
358 Cordón Caulle eruption and the 2006 Australia wildfire.

359 Most volcanic eruptions show a gradual increase in AOD over few months before
360 reaching its maximum because of the time required for aerosol dynamical processing
361 and to transform sulfur dioxide into sulfate, which usually is the main component of the
362 aerosol from volcanic eruptions. Notable exceptions are the 2022 Hunga Ha’apai and
363 the 2011 Puyehue-Cordón Caulle eruptions (Figure 23). The aerosol of the latter
364 eruption mainly consisted of volcanic ash (Vernier et al., 2013) and the former by
365 aerosol containing sulfate and sea-salt from volcanism – sea interaction (Martinsson et

366 al., 2025). These eruptions are thus less influenced by delay in aerosol formation from
 367 chemical transformation. The wildfires in the years 2009, 2017, 2019 and 2020 also
 368 rapidly reach the maximum AOD before a decline due to photolysis of organic
 369 compounds ~~with a half-life of ten days~~ reduces the AOD by 90% (Martinsson et al.,
 370 2022; Friberg et al., 2023).



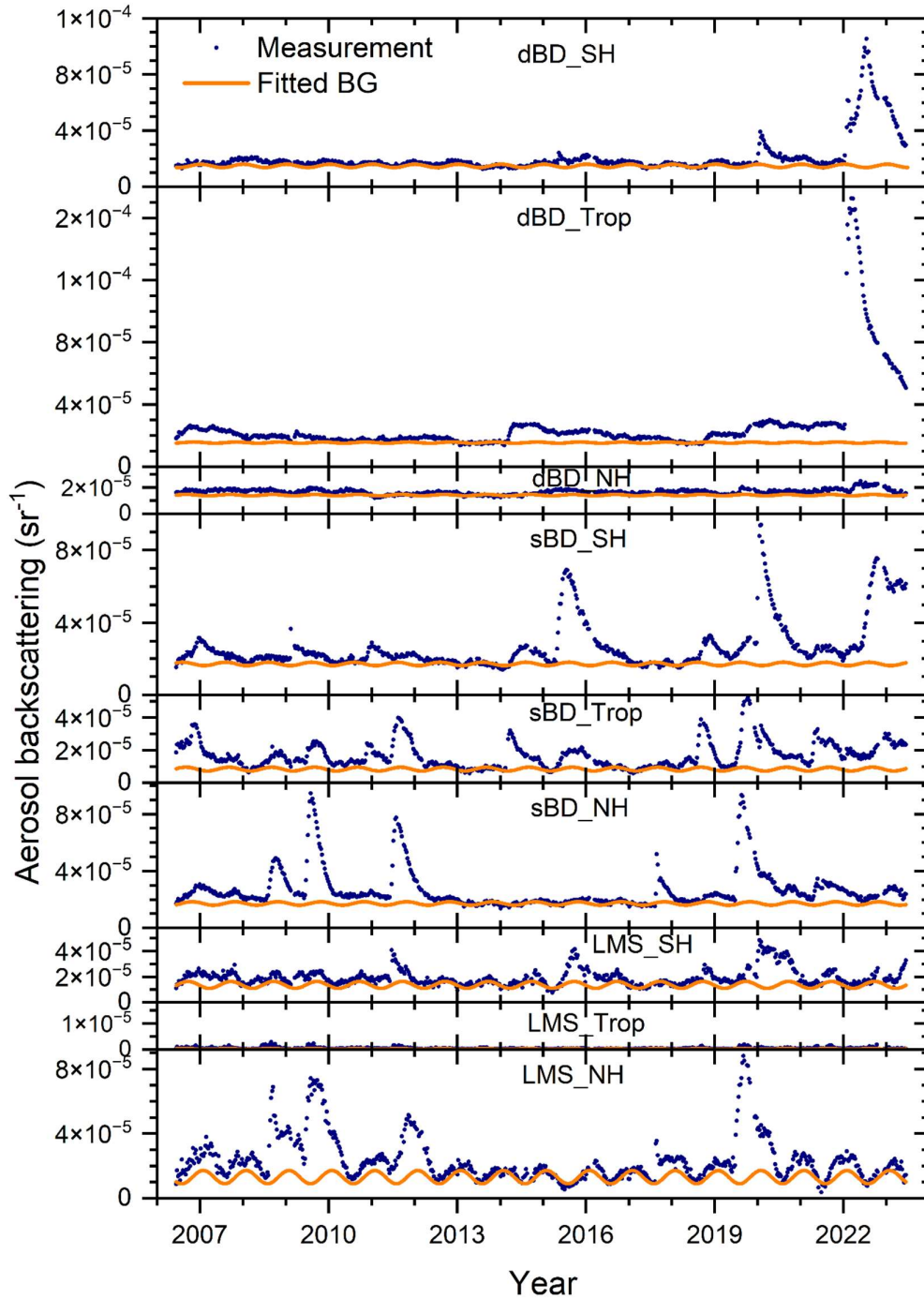
371

372 **Figure 46.** Average backscattering, which when multiplied with the lidar ratio becomes
 373 the AOD of the layer, of the background aerosol extracted based on the three lowest
 374 average values of each 8-day period over the year in the CALIOP era (2006 – 2023). The
 375 extracted data were fitted to a constant and a sinusoidal function. (Exceptions: the two
 376 lowest 8-day averages were used for “dBD_Trop” and “sBD_Trop” due to infrequent
 377 background values.) The extraction was undertaken in nine regions spanned by
 378 latitudes: -80 to -20° (SH), -20 to 20° (Tropics), 20 to 80° (NH) and altitude ranges: the
 379 tropopause to 380 K isentrope (LMS), 380 to 470 K isentrope (sBD), 470 K to 35 km
 380 altitude (dBD). The data were latitude weighted in the way that the sum of the nine
 381 layers is the global aerosol backscattering.

382

4. Discussion

383 ~~We discuss separation of aerosol signals of aerosol events due to volcanic eruptions~~
 384 ~~and wildfires from signals due to stratospheric background aerosol. This is followed by~~
 385 ~~sections on corrections of AOD due to lidar ratio deviations from the commonly~~



386

387 **Figure 57.** Stratospheric aerosol average backscattering, which when multiplied with
 388 the lidar ratio becomes the AOD, and fitted background in nine latitude and altitude
 389 regions: the deep BD branch (470 K isentrope to 35 km altitude), the shallow BD branch

390 (between isentropes 380 and 470 K) and the LMS (from the tropopause to the 380 K
391 isentrope) and three latitude regions the southern hemisphere extratropics (-80 to -20°),
392 the tropics (-20 to 20°) and the northern hemisphere extratropics (20 to 80°) to find time-
393 sections not or weakly affected by stratospheric aerosol events (see Fig. 4 and text for
394 details).

395 ~~assumed 50 sr. Then we overview the AOD and climate impact and, finally, discuss the~~
396 ~~validity of AODs from CALIOP relative to solar occultation-based instruments.~~

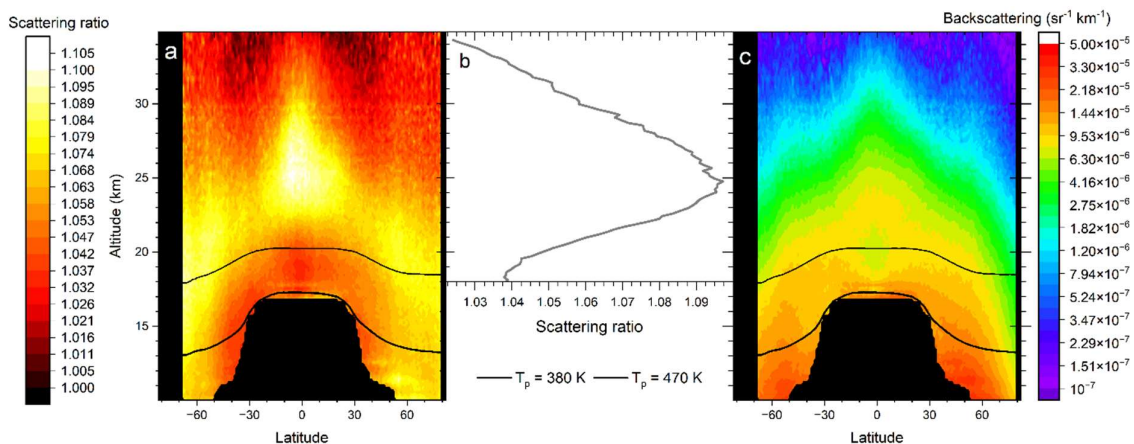
397 **4.13.3 Stratospheric background**

398 The stratospheric background aerosol is not a well-defined concept. One way is to
399 include all but major aerosol events in the background to obtain a persistently variable
400 background (Solomon et al., 2011). An alternative background is based on SAGE II
401 measurements in the volcanically quiescent period in the late 1990s to early 2000s
402 (Kremser et al., 2016). CALIOP measurements were not available in those years. A
403 volcanic eruption or wildfire rarely affects the entire stratosphere. Therefore, we divided
404 the stratosphere into nine sections by altitude and latitude thereby increasing the
405 probability of finding conditions close to background separately in each of the layers
406 using the average of the three lowest average backscattering values (in two cases the
407 two lowest) of each layer over the year (Figure 46), as described in the methods section.

408 The distribution of aerosol over the nine layers used to extract the background aerosol is
409 shown in Table 2. Seven of the nine layers each contain 11 – 15% of the background
410 aerosol in the stratosphere from the tropopause to 35 km altitude during conditions that
411 are close to background. The smallest contribution comes from the tropical LMS, which
412 is to be expected given the small air volume of that layer. The tropical sBD also has a
413 small contribution, but that cannot be explained by the air volume. This layer where
414 tropospheric air enters the stratosphere extends to approximately 20 km altitude, where
415 UV radiation intensity is too weak to efficiently oxidize carbonyl sulfide (Weisenstein et
416 al., 1997), which is an important precursor gas of the stratospheric background aerosol
417 (Crutzen, 1976; Kremser et al., 2016), a topic we return to below. Seasonal changes in
418 aerosol background average backscattering are most pronounced in the extratropical
419 LMS, especially in the NH. The volume of LMS varies over the year. That variation
420 (Appenzeller et al., 1996) approximately coincides with the variation in Figure 46 both in
421 terms of seasonality and the stronger amplitude in the LMS of the NH. ~~This is also~~

422 connected to aerosol concentrations of the LMS. In addition to the size of the LMS,
 423 seasonality of the backscattering intensity is connected to a variability in aerosol load.
 424 Poleward transport in the BD circulation maximizes in the winter resulting in increased
 425 extratropical downward motion of the stratospheric aerosol layer in the spring resulting
 426 in low aerosol load in the summer LMS when the mass transport across its upper
 427 boundary is at its minimum. The latter also coincides with the weakening of the
 428 subtropical Jetstream which increases the tropospheric influence on the LMS. In the
 429 summer/early fall there is also influence from ATAL (Vernier et al., 2015) and small
 430 wildfires briefly affecting the stratosphere (Peterson et al., 2025). The chemical
 431 composition of the LMS aerosol of the Northern hemisphere in that period differs from
 432 winter/spring/early summer by having a larger carbon than sulfur content (Martinsson et
 433 al., 2019). The change in composition can be caused by the ATAL and/or small wildfires
 434 which thus contribute to the effect of the large-scale stratospheric circulation in the
 435 build-up of the NH LMS aerosol load during late summer and fall.

436 The average backscattering of the stratospheric aerosol and the estimated background
 437 (Figure 46) in nine altitude and latitude layers is shown in Figure 57. By comparing these
 438 two quantities, we verify the underlying assumption in the method used to obtain the
 439 background that the stratospheric aerosol background has no long-term trend, which
 440 agrees with previous observations (Kremser et al., 2016). Subtracting the background,



441

442 **Figure 68.** The stratospheric aerosol averaged over year 2013, which was close to
 443 background conditions. a) The scattering ratio, i.e., the ratio between the total to the
 444 modeled backscattering of air molecules. This intensive parameter is not latitude
 445 weighted. b) Average scattering ratio in the central tropics (latitudes -10 to 10°)

446 dependence on altitude. c) Average aerosol backscattering, this extensive quantity is
 447 latitude weighted. Black lines in a) and c) are the yearly average positions of the
 448 potential temperatures (T_p) 380 and 470 K.

449

450 we obtain the average backscattering from volcanic eruptions and wildfires. The net
 451 average backscattering of the layers was converted to AOD of the layers by
 452 multiplication with the lidar ratio of 50 sr in Figure S7-S8 with contributions from
 453 volcanic eruptions and wildfires as described in section 3.2.

454 Except for a tiny peak in the LMS in the Northern extratropics, 2013 is close to
 455 background conditions (Figure 57). The stratospheric background aerosol is often
 456 thought of as a layer located above 20 km altitude in the tropics and lower in the
 457 extratropics. This is approximately true in terms of scattering ratio (R), the optical
 458 equivalent of mixing ratio (Figure 6a8a). More than half of the air entering the tropical
 459 stratosphere is transported polewards in the sBD (Lin and Fu, 2013), where the
 460 scattering ratio remains low in a band closest to the tropopause (Figure 6a8a). This band
 461 contains young stratospheric air compared to air at the same altitude but at higher
 462 latitude (Austin and Li, 2006; Butchart, 2014; Ploeger et al., 2021). In the air rising
 463 further in the tropical stratosphere a dramatic increase of the aerosol mixing ratio can
 464 be seen above 20 km altitude. The aerosol signal increases by a factor 2.5 (Figure 6b8b)
 465 from 19 to 25 km altitude in the latitude range -10 to 10°, i.e., 70% of the aerosol at 25
 466 km is formed above 19 km altitude. The dBD air is transported polewards and descends
 467 at higher latitudes than the sBD air (Figure 6a8a). With a typical vertical

468 **Table 2.** Average backscattering of background aerosol and AOD of aerosol events in
 469 2006 - 2023 and the distribution over nine stratospheric layers.

Backscattering background ^a				
	<i>Global</i>	SH	Tropics	NH
<i>Total</i>		40%	21%	39%
dBD	39%	13%	14%	12%
sBD	37%	15%	7.3%	15%
LMS	24%	12%	0.2%	11%
AOD aerosol events ^b				
	<i>Global</i>	SH	Tropics	NH
<i>Total</i>		33%	31%	35%

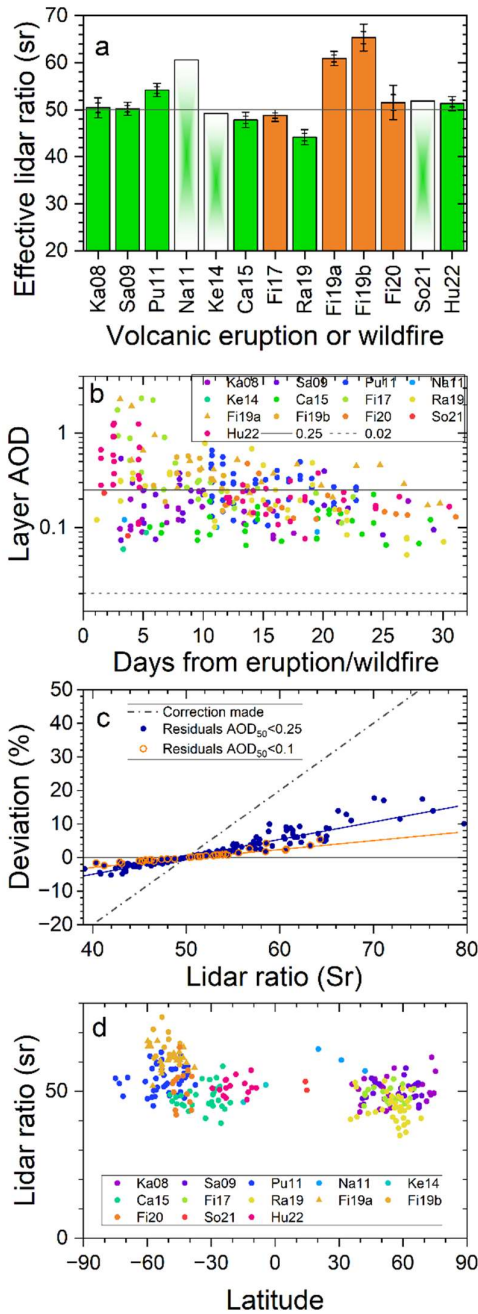
dBD	31%	9.0%	18%	4.0%
sBD	43%	15%	13%	15%
LMS	26%	9.0%	0.4%	17%

470 ^aAverage backscattering of background = 0.00011 sr⁻¹

471 ^bAverage AOD from aerosol events (2006 – 2023) = 0.0031

472

473 velocity of 20 m/day (Mote et al., 1998) the transport from the tropical tropopause (at 17
474 km) to 19 km altitude requires approximately 100 days, providing ample time for
475 conversion of SO₂ before reaching the latter altitude (Nicknish et al., 2025). Hence, little
476 SO₂ enters the dBD, implying particle formation from another source. Intensifying UV
477 radiation with altitude causes oxidation of the most abundant sulfur compound in the
478 atmosphere, i.e., carbonyl sulfide (OCS) (Crutzen, 1976; Kremser et al., 2016), whereas
479 this compound remains intact in the sBD. The requirement of intense UV radiation for
480 oxidation makes OCS an important aerosol formation pathway mainly in the dBD. The
481 formed aerosol is transported polewards where downward transport brings the aerosol
482 to the sBD and LMS layers before the transport out of the stratosphere (Figure 6a8a).
483 The formation pathways of the stratospheric background aerosol are still debated. The
484 estimated contribution of OCS to the stratospheric background aerosol ranges from 20
485 – 50% (Sheng et al., 2015; Chin and Davies, 1995) to 70% or more (Crutzen, 1976; Brühl
486 et al., 2012). High-resolution lidar data, like that of CALIOP, can be used to constrain
487 modeling efforts [to quantify sulfurous aerosol sources](#) by reconstructing the CALIOP
488 observations in Figure 6-8 to understand the sources of the background aerosol.
489 When instead considering the absolute background aerosol load (Figure 6e8c) we find
490 the highest aerosol load at low stratospheric altitudes. The air in the Brewer-Dobson



491

492 **Figure 79.** a) Average lidar ratios according to Fig. 2 with standard errors and 95%
 493 ranges of volcanic eruptions and wildfires. Too few observations for error estimations
 494 were obtained for the eruptions of Nabro (Na11), Kelut (Ke14) and Soufriere (So21). b)
 495 AODs of aerosol layers with $dS/dR \times \sigma(R) < 10$ sr Vs. time from the eruption or wildfire.
 496 The full line illustrates approximate maximum layer AOD after 1 month, and the broken
 497 line indicates the approximate maximum layer AOD observable by limb-viewing
 498 techniques (note: logarithmic y-scale). c) Correction of AOD obtained by setting the
 499 lidar ratio to 50 sr (AOD_{50}), based on a linear dependence of the AOD on the lidar ratio.
 500 The residual deviation after the correction of two categories is also shown: aerosol
 501 layers with $AOD_{50} < 0.1$ and < 0.25 . d) Estimated lidar ratios in Figure 2 Vs. latitude.

502 circulation becomes compressed during the downwelling in the extratropics in
503 accordance with the altitude-dependence of the atmospheric pressure. Mixing across
504 the extratropical tropopause culminating in the late summer with the ATAL affects the
505 aerosol load in the LMS but does not affect the mixing ratios appreciably (Figure 8a).
506 However, somewhat higher scattering ratios are found in the ATAL region (15 – 45° N and
507 13 – 18 km altitude (Vernier et al., 2015)) compared with the same region of the
508 southern hemisphere. In monthly resolution, rather than the yearly resolution of Figure
509 8, enhanced aerosol load in the ATAL area is clearly visible in July – September 2013
510 (Martinsson et al., 2017). During background conditions approximately 60% of the
511 aerosol backscattering signal (AOD divided by the lidar ratio) is found in the two lower
512 layers, sBD and LMS (Table 2), containing aerosol transported from both the sBD and
513 dBD of the tropics.

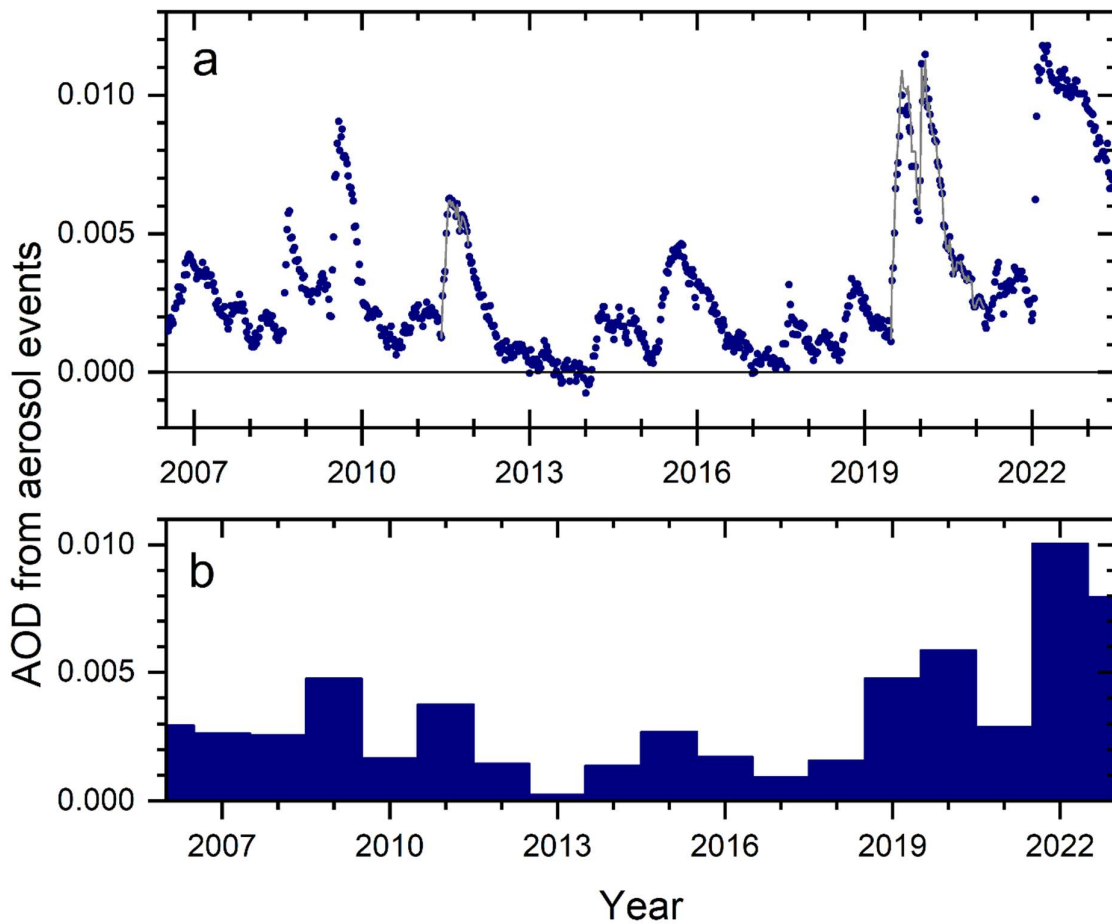
514 **4.23.4 Correction of lidar ratio**

515 Thus far we have presented AODs with the lidar ratio set to 50 sr. The lidar ratios of the
516 individual measurements are shown in Figure 2. In Figure 79a we show the averages
517 with statistical uncertainty (standard error and double-sided 95% confidence interval).
518 As already pointed out, three of the eruptions (Nabro 2011, Kelut 2014 and Soufriere
519 2021) cannot be evaluated statistically due to few available measurements. Most of the
520 aerosol events show effective lidar ratios of approximately 50 sr, whereas the aerosol
521 from Puyehue-Cordón Caulle (2011), Raikoke (2019) and the Australian wildfires in the
522 end of 2019 deviates from 50 sr by more than 5%.

523 To convert the AOD obtained using $S_0 = 50$ sr to the estimated lidar ratio (S) we need to
524 consider the linear dependence of the AOD on the lidar ratio. A secondary effect relates
525 to the level of AOD. For the latter, we need to evaluate the occurrence of dense aerosol
526 layers. All the measurements fulfilling the criteria on uncertainty of the lidar ratio
527 estimate (Figure 1) are displayed in Figure 79b. Initially layer AODs sometimes exceed 1.
528 After 20 days the AOD of the individual aerosol layers is mostly 0.25 and lower, except
529 for the 2019 Australian wildfire that remain somewhat higher probably due to less air
530 mixing in the vortex formed (Kablick et al., 2020). We corrected the AODs by S/S_0 for
531 volcanic eruptions and wildfires that formed an aerosol with effective lidar ratio
532 deviating more than 5% from $S_0 = 50$ sr, whereas the residual correction connected with

533 the AOD of an aerosol layer was not accounted for (see the methods section for further
 534 detail) because the effect is small (Figure 7e9c). In the general evaluation we did not
 535 separate the aerosol backscattering from the 2019 and 2020 Australian wildfires that
 536 were only a few days apart. The 2020 fire was dominant in terms of AOD with 80 – 90%
 537 of the total AOD from the two fires (Friberg et al., 2023). Here, we weigh the lidar ratios
 538 of the two fires accordingly to obtain $S = 53.3$ representing both fires.

539



540

541 **Figure 810.** Background-subtracted AOD of the stratosphere from the tropopause to 35
 542 km altitude and averaged from -80 to 80° in latitude. a) AOD from main stratospheric
 543 aerosol events caused by volcanic eruptions and wildfires. AOD_{50} is shown (full grey
 544 line) where correction due to lidar ratio deviating from 50 sr is undertaken (Pu11, Ra19
 545 and Fi19&20). b) Yearly averages of data in a). Note that the horizontal tick marks
 546 indicate start of a year in a) and the middle of a year in b). Also note that the averages of
 547 years 2006 and 2023 span only half years due to the mid-year start (2006) and finish
 548 (2023) of the CALIOP measurements.

550 The blue dots in Figure 810a over the stratospheric AOD were corrected for deviant lidar
 551 ratios in 2011 (Puyehue-Cordón Caulle eruption by +8%) and 2019 – 2020 (Raikoke
 552 eruption by -12% and Australian wildfires by +7%). The corresponding AOD using $S_0 = 50$
 553 sr is represented by a thin gray line showing that the AOD was practically not affected by
 554 the correction in 2011 because that year was dominated by aerosol from another
 555 eruption (Nabro, Figure 3). The AOD from the Raikoke (2019) eruption shifted down
 556 slightly by the correction, and that of the 2019 – 2020 Australian wildfires shifted
 557 upwards.

558 Altogether the changes in AOD from the corrections due to deviant lidar ratio were
 559 found to be minor, the largest correction (-12%) was applied to the AOD of the Raikoke
 560 eruption. However, we could not statistically quantify all major aerosol events, most
 561 notably the Nabro eruption in 2011 (Figure 2). Our results show that assumption of an
 562 effective lidar ratio of 50 sr works satisfactory in most cases in the 17-year period
 563 studied when the stratospheric aerosol is influenced by volcanism or wildfires. The
 564 applied method to obtain the effective lidar ratio cannot be used for optically thin layers
 565 like the background aerosol.

566 **4.33.5 AOD of stratospheric aerosol events**

567 The AOD from aerosol events were approximately evenly distributed over the three
 568 latitude regions (SH, Tropics and NH-80 to -20°, -20 to 20° and 20 to 80°) studied (Table
 569 2). The altitude distribution showed most influence from volcanic eruptions and
 570 wildfires in the sBD (43%), followed by the dBD (31%), and the often overlooked LMS
 571 (Andersson et al., 2015) held 26% of the AOD from aerosol events in the period 2006 –
 572 2023.

573 The average stratospheric AOD, with the contribution from background aerosol
 574 subtracted, from the tropopause to 35 km altitude in the latitude range -80 to 80° is
 575 shown in Figure 810a. The intense volcanism – sea interaction of the Hunga Ha’apai
 576 eruption in the beginning of 2022 (Martinsson et al., 2025) resulted in the highest and
 577 broadest AOD peak (Figure 810a). Other prominent events were the Australian wildfires
 578 at the end of 2019 and the beginning of 2020, the eruptions of Raikoke (2019), Sarychev

579 (2009), Nabro (2011), Calbuco (2015) and Kasatochi (2008) affecting the stratospheric
580 AOD together with several eruptions and wildfires having smaller contributions (Table
581 1).

582 The average influence of volcanic eruptions and wildfires each year is shown in Figure
583 810b. The most affected year was 2022 with an average AOD of 0.01 from aerosol
584 events. That year is likely followed by 2023, for which we have no data from the second
585 half of the year. Both these years were mainly affected by the 2022 Hunga Ha’apai
586 eruption. Then follows 2020 (mainly the 2019-20 Australian wildfires with some
587 contribution from the Raikoke eruption) with background-subtracted AOD of 0.006,
588 2009 (Sarychev) and 2019 (Raikoke) both years with AOD of 0.005, whereas 2011
589 (mainly Nabro) reach AOD from aerosol events of almost 0.004. The average
590 background-subtracted AOD from volcanic eruptions and wildfires from 2006 to 2023 is
591 0.0031. The background aerosol produces global average backscattering of 0.00011 sr^{-1} ,
592 which, with the commonly used assumption of a lidar ratio of 50 sr, corresponds to a
593 stratospheric background AOD of 0.0057.

594 The yearly average AOD from aerosol events ranges from 0.0002 (in 2013) to 0.010
595 (2022) and the average over the 17 years studied is 0.0031. Making use of previous
596 estimates of the relation between radiative forcing (F) and stratospheric AOD ($F = -$
597 $24 \times \text{AOD}$ in W/m^2) (Schmidt et al., 2018), we can obtain a first, simplified estimate of the
598 radiative effect of the stratospheric aerosol events. This relation is based on volcanic
599 sulfate aerosol, which is the dominant type of stratospheric aerosol event in the 17-year
600 period studied. The relation is not designed to deal with absorbing wildfire aerosol,
601 which could cause some uncertainty in the average radiative forcing of the period
602 estimated here. This simplified estimate of F the global stratospheric yearly average total
603 effective radiative forcing due to volcanic eruptions and wildfires varies between -0.006
604 and -0.24 W/m^2 , with the average -0.074 W/m^2 in the period 2006 to 2023. Assuming a
605 lidar ratio of 50 sr, the stratospheric background aerosol effective radiative forcing
606 becomes -0.14 W/m^2 .

607 4. Discussion

608 **4.4 The validity of AODs from CALIOP**

609 Stratospheric aerosol optical properties are often described using solar occultation
610 data, especially from the 22 years of SAGE II measurements (Bauman et al., 2003;
611 Thomason et al., 2018). Prior comparisons of CALIOP lidar-based results with solar
612 occultation (SAGE III/ISS) show agreement within approximately 10% in the latitude
613 range -30 to 30° and increasing discrepancy at midlatitudes reaching above 50% at high
614 latitudes for background aerosol in the altitude range 20 – 30 km (Kar et al., 2019), and
615 discrepancies exceeding 50% is reported at altitudes below 17 km (Kovilakam et al.,
616 2023). The main reason for these differences was attributed to the unknown lidar ratio
617 of CALIOP (Kar et al., 2019; Kovilakam et al., 2023). Here we have estimated the CALIOP
618 effective lidar ratio of the aerosol from several volcanic eruptions and wildfires (Figure
619 2), and in Figure 7d-9d the latitude distribution of the estimates is shown. Using the
620 standard lidar ratio of 50 sr cannot explain the latitude- and altitude-dependence in the
621 lidar – solar occultation comparison obtained in Kar et al. (2019) and Kovilakam et al.
622 (2023) for aerosol from volcanic eruptions and wildfires in the CALIOP era.

623 The latitude-dependent discrepancy at 532 nm wavelength between SAGE III/ISS and
624 CALIOP at high altitudes in the period June 2017 to August 2018 above 20 km (, i.e.,
625 essentially in the dBD) reported by Kar et al. (2019) concerns a period when the dBD
626 was close to background (Figure 57). The method used here for estimating the lidar ratio
627 does not work for background conditions (Figure 1). Using ~~50 sr~~ the standard CALIOP
628 lidar ratio for the background aerosol (50 sr) results in the global average background
629 AOD of 0.0057. SAGE II measurements during the volcanically quiescent period 1998 –
630 2000 resulted in AOD of 0.0040 (estimated from Solomon et al. (2011), their Figure 2),
631 who integrated the stratospheric AOD from 15 km altitude. When removing the
632 stratospheric aerosol data below 15 km from the CALIOP measurements, the
633 stratospheric background AOD is reduced by 31% to 0.0039 using lidar ratio 50 sr. This
634 is almost identical to the background AOD reported in Solomon et al. (2011), thus
635 indicating that the stratospheric background aerosol on average has a lidar ratio close
636 to 50 sr. Kar et al. (2019) found that aerosol backscattering during background
637 conditions at altitudes above 20 km in the extratropics should be converted to AOD by a
638 variable lidar ratio. Mid- and high-latitude air in this altitude range has a high

639 stratospheric age (~5 years) (Ploeger et al., 2021), implying that particle ~~gravitational~~
640 settling has long time to affect the ~~particle~~ size distribution, and hence the optical
641 properties of the aerosol. In Figure ~~6c-8c~~ we find most of the aerosol above 20 km
642 altitude ~~to be located~~ in the tropics, implying that the deviations at high latitudes
643 ~~according to that~~ Kar et al. (2019) ~~reported~~ have little impact on global AOD, and thus
644 little impact on our comparison ~~with Solomon et al. (2011) that~~ dealing with the entire
645 stratosphere above 15 km altitude.

646 In a comparison by Kovilakam et al. (2023) between CALIOP and SAGE III/ISS during
647 November 2017, 2 – 3 months after the Canada/USA fire (Table 1) large deviations were
648 found at high latitudes and altitudes as in Kar et al. (2019), as described above. ~~That~~
649 ~~comparison Kovilakam et al. (2023)~~ also found large differences in the densest part of
650 the stratosphere, ~~i.e., at altitudes below 17 km, where clouds frequently interfere with~~
651 ~~limb-viewing measurements~~. In GloSSAC the more than 50% lower values of limb-
652 viewing techniques (SAGE and OSIRIS) than CALIOP were ~~implemented adopted,~~
653 ~~justified by~~ citing uncertainties in the lidar ratio to discard CALIOP results at low
654 altitudes (Kovilakam et al., 2023).

655 The main advantages of solar occultation measurements are that extinction is
656 measured and that several wavelengths are available. ~~With known lidar ratio, t~~Lidar
657 measurements ~~also have some distinct advantages. with nadir view have some distinct~~
658 ~~advantages compared to solar occultation limb views. Firstly, t~~Lidars ~~with nadir view~~
659 have several hundred kilometers shorter measurement path enabling measurements in
660 dense aerosol layers (Martinsson et al., 2022, their Figure 7) ~~providing producing~~ viable,
661 quantitative results when limb views fail, ~~provided that the lidar ratio is known~~.
662 ~~Secondly, t~~The lidar vertical resolution is superior and is not relying on assumptions on
663 homogeneity of the aerosol layer measured, like solar occultation measurements do
664 (Damadeo et al., 2013). Accurate altitude descriptions with high vertical resolution of
665 stratospheric injections (Sandvik et al., 2021) ~~is-are~~ vital for the outcome of
666 stratospheric aerosol modeling (Axebrink et al., 2025). ~~With these clear~~
667 ~~advantages Relying on these points~~ we argue that ~~the role of~~ lidar measurements should
668 be ~~given a more prominent role re-evaluated~~. Existing methods differ in their sensitivity
669 ~~to aerosol properties and in their temporal coverage. We need to take advantage of the~~

670 ~~best qualities of all available methods, both in terms of physical properties and time~~
671 ~~coverage. Re-evaluation of CALIOP data could improve~~ stratospheric aerosol
672 climatologies, like GloSSAC (Thomason et al., 2018, Kovilakam et al., 2020; Kovilakam
673 et al., 2023), ~~presented to that are designed for~~ the modeling community, ~~ultimately~~
674 ~~leading to a better representation of the stratospheric aerosol in climate modeling than~~
675 ~~in the present version (2.2) of GloSSAC (Thomason et al., 2018, Kovilakam et al., 2020;~~
676 ~~Kovilakam et al., 2023).~~

677 Hopefully the lidar ratio of stratospheric aerosol can be further clarified when the
678 aerosol load is close to background conditions by lidar systems measuring both
679 backscattering and extinction. The ATLID aboard the EarthCARE satellite (Illingworth et
680 al., 2015) that started to produce data in July 2024 and the NASA and Italian Space
681 Agency collaboration on the 3 wavelength lidar CALIGOLA planned for launch in the
682 early 2030s (Behrenfeld et al., 2023) are future means to further clarify extinction
683 obtained from lidars, and to optimally combine solar occultation and lidar
684 measurements for future long-term records on the optical properties of the
685 stratospheric aerosol with high and unambiguous vertical resolution.

686 5. Conclusions

687 The entire backscattering record at 532 nm wavelength of the satellite-based lidar
688 system CALIOP spanning years 2006 to 2023 was investigated in this study. During this
689 period injections of aerosol and precursor gases into the stratosphere of 15 volcanic
690 eruptions and 5 wildfires were identified. The effective lidar ratios of 12 volcanic
691 eruptions and wildfires were investigated to convert the measured backscattering to
692 extinction. The measurements were evaluated and corrected for attenuation using the
693 lidar ratio $S_0 = 50$ sr. The aerosol events having a lidar ratio deviating by more than 5%
694 from S_0 were corrected after the general evaluation.

695 Background aerosol conditions are more probable-likely to occur in sublayers than in
696 throughout the entire stratosphere. The stratosphere was therefore subdivided into 9
697 layers spanned by altitude (lowermost stratosphere (LMS), shallow Brewer-Dobson
698 branch (sBD), deep Brewer-Dobson branch (dBD)) and latitude intervals (tropics and

699 Southern and Northern extratropics). The backgrounds of layers were combined to
700 obtain ~~that the background aerosol~~ of the entire stratosphere. The backscattering of
701 background aerosol was converted to aerosol optical depth (AOD) using a lidar ratio of
702 50 sr. That AOD agrees well with measurements with solar occultation (SAGE II) during
703 1998 – 2000 in the volcanically quiescent period. The average backscattering of seven of
704 the nine layers each contains 11 - 15% of the entire background aerosol. The tropical
705 LMS has a small contribution due to very small volume compared to the other layers.
706 The tropical sBD was also clearly lower (7%) because oxidation of carbonyl sulfide
707 (OCS) occurs at higher altitudes in the upwards moving air in the tropical stratosphere.
708 We find that 70% of the aerosol in the tropical dBD is formed above 19 km altitude
709 during background conditions, due to formation from OCS. ~~A several kilometers thick~~
710 ~~band of low aerosol load directly above the tropopause was identified which we~~
711 ~~attribute to young stratospheric air transported in the sBD. Above that layer a broad~~
712 ~~band with high aerosol load was found which we identify as the tropical dBD air that~~
713 ~~after Ppoleward followed by downward transport of the dBD aerosol to the sBD and LMS~~
714 ~~results in high aerosol concentrations-load at mid and high latitudes, whereas the~~
715 ~~polewards transport of tropical sBD air causes a band of low concentrations close to~~
716 ~~the tropopause at lower latitudes than the dBD air.~~ Considering the ongoing debate on
717 the sources of stratospheric background aerosol, these highly resolved CALIOP data
718 could be useful to constrain modeling efforts on the ~~subjectsources of the stratospheric~~
719 ~~sulfurous aerosol.~~

720 The background aerosol ~~AOD (0.0057)~~ was subtracted from the measurements to
721 obtain the influence from aerosol and trace gas injections into the stratosphere. The
722 most important aerosol events in the 17-year period are the 2022 Hunga Ha’apai
723 eruption and the Australian wildfires (2019-20) followed by the volcanic eruptions
724 Raikoke (2019), Sarychev (2009) and Nabro (2011). ~~With the background AOD (0.0057)~~
725 ~~subtracted, t~~The ~~global~~ yearly average AOD ~~increase from volcanic and wildfire~~
726 ~~injections~~ spans 0 to 0.010. ~~Using a simplified relation the yearly average effective~~
727 ~~radiative forcing of the background-subtracted aerosol is estimated to be in the range-~~
728 ~~0.006 (year 2013) to -0.24 W/m² (2022).~~

729 Limb-viewing solar occultation measurements have some distinctive advantages in that
730 much of the early measurements in the satellite era were undertaken with that method.
731 They also deliver direct measurements of extinction, and at several wavelengths. Here,
732 we have estimated the effective lidar ratio of the CALIOP measurements to obtain
733 extinction from backscattering measurements. Lidars operating in nadir view, like
734 CALIOP, have several hundred kilometers (or a factor of more than 100) shorter
735 measurement path than limb-viewers, allowing measurements in dense aerosol layers
736 where limb-viewers fail. Lidars have unambiguous and superior vertical resolution over
737 other satellite instruments providing models with important input ~~data-ofon~~ aerosol and
738 trace gas injections into the stratosphere. Newer lidars that measure extinction are
739 launched, under construction and planned. Now is the time to better sort out
740 differences between lidars and solar occultation measurements., With known effective
741 lidar ratios the relation between CALIOP and solar occultation measurements need to
742 be re-evaluated, especially in the dense stratospheric air located below 17 km altitude
743 in long-term records over the optical properties of the stratospheric aerosol.

744 **References**

- 745 Andersson, S. M., Martinsson, B. G., Friberg, J., Brenninkmeijer, C. A. M., Rauthe-
746 Schöch, A., Hermann, M., van Velthoven, P. F. J., and Zahn, A.: Composition and
747 evolution of volcanic aerosol from eruptions of Kasatochi, Sarychev and
748 Eyjafjallajökull in 2008–2010 based on CARIBIC observations, *Atmos. Chem.*
749 *Phys.*, 13, 1781–1796, <https://doi.org/10.5194/acp-13-1781-2013>, 2013.
- 750 Andersson, S. M., Martinsson, B. G., Vernier, J.-P., Friberg, J., Brenninkmeijer, C. A. M.,
751 Hermann, M., van Velthoven, P. F. J., and Zahn, A.: Significant radiative impact of
752 volcanic aerosol in the lowermost stratosphere, *Nat. Commun.*, 6, 1–8,
753 <https://doi.org/10.1038/ncomms8692>, 2015.
- 754 Appenzeller, C., Holton, J.R., and Rosenlov, K.H.: Seasonal variation of mass transport
755 across the tropopause, *J. Geophys. Res.* 101, 15071-15078, 1996.
- 756 Austin, J., and Li, F.: On the relationship between the strength of the Brewer-Dobson
757 circulation and the age of stratospheric air, *Geophys. Res. Lett.*, 33, L17807,
758 [doi:10.1029/2006GL026867](https://doi.org/10.1029/2006GL026867), 2006.
- 759 Axebrink, E., Sporre, M.K., and Friberg, J.: Impact of SO₂ injection profiles on simulated
760 volcanic forcing for the 2009 Sarychev eruptions– investigating the importance of
761 using high-vertical-resolution methods when compiling SO₂ data, *Atmos. Chem.*
762 *Phys.*, 25, 2047–2059, <https://doi.org/10.5194/acp-25-2047-2025>, 2025.

- 763 Bauman, J. J., Russell, P. B., Geller, M. A., and Hamill, P.: A stratospheric aerosol
764 climatology from SAGE II and CLAES measurements: 2. Results and
765 comparisons, 1984–1999, *J. Geophys. Res.*, 108, 4383,
766 <https://doi.org/10.1029/2002JD002993>, 2003.
- 767 Behrenfeld, M.J., Lorenzoni, L., Hu, Y., Bissom, K.M., Hostetler, C.A., Di Girolamo, P.,
768 Dionisi, D., Longo, F., and Zoffoli, S.: Satellite Lidar Measurements as a Critical
769 New Global Ocean Climate Record, *Remote Sens.* 15, 5567. <https://doi.org/10.3390/rs15235567>, 2023.
- 771 Brühl, C., Lelieveld, J., Crutzen, P.J., and Tost, H.: The role of carbonyl sulphide as a
772 source of stratospheric sulphate aerosol and its impact on climate, *Atmos.*
773 *Chem. Phys.*, 12, 1239–1253, www.atmos-chem-phys.net/12/1239/2012/
774 [doi:10.5194/acp-12-1239-2012](https://doi.org/10.5194/acp-12-1239-2012), 2012.
- 775 Butchart, N., The Brewer-Dobson circulation, *Rev. Geophys.*, 52, 157–184,
776 [doi:10.1002/2013RG000448](https://doi.org/10.1002/2013RG000448), 2014.
- 777 Carn, S.A., Krueger, A.J., Krotkov, N.A., Yang, K., and Evans, K.: Tracking volcanic sulfur
778 dioxide clouds for aviation hazard mitigation, *Nat Hazards*, 51, 325–343 DOI
779 [10.1007/s11069-008-9228-4](https://doi.org/10.1007/s11069-008-9228-4), 2009.
- 780 Carn, S.A., and Prata, F.J., Satellite-based constraints on explosive SO₂ release from
781 Soufrière Hills Volcano, Montserrat, *Geophys. Res. Lett.*, 37, 1-5, L00E22,
782 [doi:10.1029/2010GL044971](https://doi.org/10.1029/2010GL044971), 2010.
- 783 Carn, S. A., Krotkov, N. A., Fisher, B. L., and Li, C.: Out of the blue: Volcanic SO₂
784 emissions during the 2021–2022 eruptions of Hunga Tonga– Hunga Ha’apai
785 (Tonga), *Front. Earth Sci.*, 10, 976962,
786 <https://doi.org/10.3389/feart.2022.976962>, 2022.
- 787 Chin, M., and Davies, D.D.: A reanalysis of carbonyl sulfide as a source of stratospheric
788 background sulfur aerosol, *J. Geophys. Res.* 100, 8993-9005, 1995.
- 789 Clarisse, L., Hurtmans, D., Clerbaux, C., Hadji-Lazaro, J., Ngadi, Y., and Coheur, P.-F.:
790 Retrieval of sulphur dioxide from the infrared atmospheric sounding
791 interferometer (IASI), *Atmos. Meas. Tech.*, 5, 581–594,
792 <https://doi.org/10.5194/amt-5-581-2012>, 2012.
- 793 Clarisse, L., Coheur, P.-F., Prata F., Hadji-Lazaro, J., Hurtmans, D., and Clerbaux, C.: A
794 unified approach to infrared aerosol remote sensing and type specification,
795 *Atmos.Chem.Phys.*, 13, 2195–2221, www.atmos-chem-phys.net/13/2195/2013/
796 [doi:10.5194/acp-13-2195-2013](https://doi.org/10.5194/acp-13-2195-2013), 2013.
- 797 Crutzen, P.J.: The possible importance of CSO for the sulfate layer of the stratosphere,
798 *Geophys. Res. Lett.* 3, 73-76, 1976.

- 799 Cruz, M.G., Sullivan, A.L., Gould, J.S., Sims, N.C., Bannister, A.J., Hollis, J.J., and Hurley,
800 R.J.: Anatomy of a catastrophic wildfire: The Black Saturday Kilmore East fire in
801 Victoria, Australia, *Forest Ecol. Manag.* 284, 269-295, 2012.
- 802 Damadeo, R.P., Zawodny, J.M., Thomason, L.W., and Iyer, N.: SAGE version 7.0
803 algorithm: application to SAGE II, *Atmos. Meas. Tech.*, 6, 3539–3561,
804 www.atmos-meas-tech.net/6/3539/2013/, 2013.
- 805 Friberg, J., Martinsson, B. G., Andersson, S. M., Brenninkmeijer, C. A. M., Hermann, M.,
806 Van Velthoven, P. F. J., and Zahn, A.: Sources of increase in lowermost
807 stratospheric sulphurous and carbonaceous aerosol background concentrations
808 during 1999–2008 derived from CARIBIC flights, *Tellus B*, 66, 23428,
809 <https://doi.org/10.3402/tellusb.v66.23428>, 2014.
- 810 Friberg, J., Martinsson, B. G., Andersson, S. M., and Sandvik, O. S.: Volcanic impact on
811 the climate– the stratospheric aerosol load in the period 2006–2015, *Atmos.*
812 *Chem. Phys.*, 18, 11149–11169, <https://doi.org/10.5194/acp-18-11149-2018>,
813 2018.
- 814 Friberg, J., Martinsson, B. G., and Sporre, M. K.: Short- and long-term stratospheric
815 impact of smoke from the 2019–2020 Australian wildfires, *Atmos. Chem. Phys.*,
816 23, 12557–12570, <https://doi.org/10.5194/acp-23-12557-2023>, 2023.
- 817 Fromm, M., Lindsey, D. T., Servranckx, R., Yue, G., Trickl, T., Sica, R., Doucet, P., and
818 Godin-Beekmann, S.: The untold story of pyrocumulonimbus, *B. Am. Meteorol.*
819 *Soc.*, 91, 1193–1209, 2010.
- 820 Fromm, M., Kablick III, G. P., Peterson, D. A., Kahn, R. A., Flower, V. J. B., and Seftor, C. J.:
821 Quantifying the source term and uniqueness of the August 12, 2017 Pacific
822 Northwest pyroCb event, *J. Geophys. Res.*, 126, e2021JD034928,
823 <https://doi.org/10.1029/2021JD034928>, 2021.
- 824 Garofalo, L. A., Levin, E. J. T., Campos, T., Kreidenweis, S. N., and Farmer, D. K.:
825 Emission and evolution of submicron organic aerosol in smoke from wild fires in
826 the western United States, *ACS Space Chem.*, 3, 1237–1247, 2019.
- 827 Gelaro, R., McCarty, W., Suarez, M. J., Todling, R., Moloud, A., Takacs, L., Randles, C. A.,
828 Darmenov, A., Bosilovich, M. G., Reichle, R., Wargan, K., Coy, L., Cullather, R.,
829 Draper, C., Akella, S., Buchard, V., Conaty, A., da Silva, A. M., Gu, W., Kim, G.-K.,
830 Koster, R., Lucchesi, R., Merkova, D., Nielsen, J. E., Partyka, G., Pawson, S.,
831 Putman, W., Rienecker, M., Schubert, S. D., Seinkiewicz, M., and Zhao, B.: The
832 Modern-Era Retrospective Analysis for Research and Applications, Version 2
833 (MERRA-2), *J. Clim.* 30, 5419-5454, 2017.
- 834 Haywood, J.M., Jones, A., Clarisse, L., Bourassa, A., Barnes, J., Telford, P., Bellouin, N.,
835 Boucher, O., Agnew, P., Clerbaux, C., Coheur, P., Degenstein, D., and Braesicke,
836 P.: Observations of the eruption of the Sarychev volcano and simulations using

837 the HadGEM2 climate model, *J. Geophys. Res.*, 115, D21212,
838 doi:10.1029/2010JD014447, 2010.

839 Illingworth, A. J., Barker, H. W., Beljaars, A., Ceccaldi, M., Chepfer, H., Clerbaux, N.,
840 Cole, J., Delanoë, J., Domenech, C., Donovan, D. P., Fukuda, S., Hirakata, M.,
841 Hogan, R. J., Huenerbein, A., Kollias, P., Kubota, T., Nakajima, T., Nakajima, T. Y.,
842 Nishizawa, T., Ohno, Y., Okamoto, H., Oki, R., Sato, K., Satoh, M., Shephard, M.
843 W., Velázquez-Blázquez, A., Wandinger, U., Wehr, T., and van Zadelhoff, G.-J.: The
844 Earth CARE Satellite: The Next Step Forward in Global Measurements of Clouds,
845 Aerosols, Precipitation, and Radiation, *B. Am. Meteorol. Soc.*, 96, 1311–1332,
846 <https://doi.org/10.1175/BAMS-D-12-00227.1>, 2015.

847 Junge, C.E., Chagnon, C.W., and Manson, J.E.: A World-wide Stratospheric Aerosol
848 Layer, *Science*, 133, 1478-1479, 1961.

849 Kablick, G. P., Allen, D. R., Fromm, M. D., and Nedoluha, G. E.: Australian PyroCb Smoke
850 Generates Synoptic-Scale Stratospheric Anticyclones, *Geophys. Res. Lett.*, 47,
851 e2020GL08810, <https://doi.org/10.1029/2020GL088101>, 2020.

852 Kar, J., Lee, K.-P., Vaughan, M. A., Tackett, J. L., Trepte, C. R., Winker, D. M., Lucker, P. L.,
853 and Getzewich, B. J.: CALIPSO level 3 stratospheric aerosol profile product:
854 version 1.00 algorithm description and initial assessment, *Atmos. Meas. Tech.*,
855 12, 6173–6191, <https://doi.org/10.5194/amt-12-6173-2019>, 2019.

856 Kloss, C., Berthet, G., Sellitto, P., Ploeger, F., Taha, G., Tidiga, M., Eremenko, M.,
857 Bossolasco, A., Jégou, F., Renard, J.-B., and Legras, B.: Stratospheric aerosol
858 layer perturbation caused by the 2019 Raikoke and Ulawun eruptions and their
859 radiative forcing, *Atmos. Chem. Phys.*, 21, 535–560, <https://doi.org/10.5194/acp-21-535-2021>, 2021.

861 Kovilakam, M., Thomason, L.W., Ernest, N., Rieger, L.A., Bourassa, A.E., and Millán, L.:
862 The Global Space-based Stratospheric Aerosol Climatology (version 2.0): 1979–
863 2018, *Earth Syst. Sci. Data*, 12, 2607–2634, <https://doi.org/10.5194/essd-12-2607-2020>, 2020.

865 Kovilakam, M., Thomason, L.W., and Knepp, T.: SAGEIII/ISS aerosol/cloud categorization
866 and its impact on GloSSAC, *Atmos. Meas. Tech.*, 16, 2709–2731,
867 <https://doi.org/10.5194/amt-16-2709-2023>, 2023.

868 Kremser, S., Thomason, L. W., von Hobe, M., Hermann, M., Desher, T., Timmreck, C.,
869 Toohey, M., Stenke, A., Schwarz, J. P., Weigel, R., Fueglistaler, S., Prata, F. J.,
870 Vernier, J. P., Schlager, H., Barnes, J. E., Antuña-Marrero, J. C., Fairlie, D., Palm,
871 M., Mahieu, E., Notholt, J., Rex, M., Bingen, C., Vanhellefont, F., Bourassa, A.,
872 Plane, J. M. C., Klocke, D., Carn, S. A., Clarisse, L., Trickl, T., Neely, R., James, A.
873 D., Rieger, L., Wilson, J. C., and Meland, B.: Stratospheric aerosol– Observations,
874 processes, and impact on climate, *Rev. Geophys.*, 54, 278–335,
875 <https://doi.org/10.1002/2015RG000511>, 2016.

- 876 Li, C., Krotkov, N.A., Carn, S., Zhang, Y., Spurr, R.D.J., and Joiner, J.: New-generation
877 NASA Aura Ozone Monitoring Instrument (OMI) volcanic SO₂ dataset: algorithm
878 description, initial results, and continuation with the Suomi-NPP Ozone Mapping
879 and Profiler Suite (OMPS), *Atmos. Meas. Tech.*, 10, 445–458, [www.atmos-meas-
880 tech.net/10/445/2017/](http://www.atmos-meas-tech.net/10/445/2017/), doi:10.5194/amt-10-445-2017, 2017.
- 881 Lin, P., and Fu, Q., Changes in various branches of the Brewer–Dobson circulation from
882 an ensemble of chemistry climate models, *J. Geophys. Res.*, 118, 73–84,
883 doi:10.1029/2012JD018813, 2013.
- 884 Malinina, E., Rozanov, A., Niemayer, U., Wallis, S., Arosio, C., Wrana, F., Timmreck, C.,
885 von Savigny, C., and Burrows, J.P.: Changes in stratospheric aerosol extinction
886 coefficient after the 2018 Ambae eruption as seen by OMPS-LP and MAECHAM5-
887 HAM, *Atmos. Chem. Phys.*, 21, 14871–14891, [https://doi.org/10.5194/acp-21-
888 14871-2021](https://doi.org/10.5194/acp-21-14871-2021), 2021.
- 889 Martinsson, B. G., Nguyen, H. N., Brenninkmeijer, C. A. M., Zahn, A., Heintzenberg, J.,
890 Hermann, M., and Velthoven, P. F. J. v.: Characteristics and origin of lowermost
891 stratospheric aerosol at northern midlatitudes under volcanically quiescent
892 conditions based on CARIBIC observations, *J. Geophys. Res.*, 110, D12201,
893 doi:10.1029/2004JD005644, 2005.
- 894 Martinsson, B. G., Brenninkmeijer, C. A. M., Cam, S. A., Hermann, M., Heue, K.P., van
895 Velthoven, P. F. J., and Zahn, A.: Influence of the 2008 Kasatochi volcanic
896 eruption on sulfurous and carbonaceous aerosol constituents in the lower
897 stratosphere, *Geophys. Res. Lett.*, 36, 1–5,
898 <https://doi.org/10.1029/2009GL038735>, 2009.
- 899 [Martinsson, B. G., Friberg, J., Sandvik, O. S., Hermann, M., van Velthoven, P. F. J., and
900 Zahn, A.: Particulate sulfur in the upper troposphere and lowermost
901 stratosphere– sources and climate forcing, *Atmos. Chem. Phys.*, 17, 10937–
902 10953, <https://doi.org/10.5194/acp-17-10937-2017>, 2017.](#)
- 903 Martinsson, B. G., Friberg, J., Sandvik, O. S., Hermann, M., van Velthoven, P. F. J., and
904 Zahn, A.: Formation and composition of the UTLS aerosol, *npj Climate and
905 Atmospheric Science*, 2, 1–6, <https://doi.org/10.1038/s41612-019-0097-1>, 2019.
- 906 Martinsson, B. G., Friberg, J., Sandvik, O. S., and Sporre, M. K.: Five-satellite-sensor
907 study of the rapid decline of wildfire smoke in the stratosphere, *Atmos. Chem.
908 Phys.*, 22, 3967–3984, <https://doi.org/10.5194/acp-22-3967-2022>, 2022.
- 909 Martinsson, B. G., Friberg, J., and Sporre, M. K.: Stratospheric aerosol formed by intense
910 volcanism–sea interaction during the 2022 Hunga Ha’apai eruption, *Atmos.
911 Chem. Phys.*, 25, 10677–10690, <https://doi.org/10.5194/acp-25-10677-2025>,
912 2025.

- 913 Mastin, L. G., Van Eaton, A. R., and Cronin, S. J.: Did steam boost the height and growth
914 rate of the giant Hunga eruption plume?, *B. Volcanol.*, 86, 64,
915 <https://doi.org/10.1007/s00445-024-01749-1>, 2024.
- 916 McCarthy, G.J., Plucinski, M.P., and Gould, J.S.: Analysis of the resourcing and
917 containment of multiple remote fires: The Great Divide Complex of fires, Victoria,
918 December 2006, *Australian Forestry*, 75, 54-63, DOI:
919 10.1080/00049158.2012.10676385, 2012.
- 920 Mote, P.W., Dunkerton, T.J., McIntyre, M.E., Ray, E.A., Haynes, P.H., and Russell III, J.M.:
921 Vertical velocity, vertical diffusion, and dilution by midlatitude air in the tropical
922 lower stratosphere, *J. Geophys. Res.* 103, 8651-8666, 1998.
- 923 Murphy, D. M., Cziczo, D. J., Hudson, P. K., and Thomson, D. S.: Carbonaceous material
924 in aerosol particles in the lower stratosphere and tropopause region, *J. Geophys.*
925 *Res.*, 112, D04203, <https://doi.org/10.1029/2006JD007297>, 2007.
- 926 NASA/LARC/SD/ASDC: Science CALIPSO Lidar Level 1B profile data, V4-51, NASA
927 Langley Atmospheric Data Center DAAC,
928 https://doi.org/10.5067/CALIOP/CALIPSO/CAL_LID_L1-Standard-V4-51, 2024.
- 929 Nicknish, P.A., Stone, K., Solomon, S., and Carn, S.A.: Quantifying the decay timescale
930 of volcanic sulfur dioxide in the stratosphere, *Atmos. Chem. Phys.*, 25, 11535–
931 11555, <https://doi.org/10.5194/acp-25-11535-2025>, 2025.
- 932 Ohneiser, K., Ansmann, A., Baars, H., Seifert, P., Barja, B., Jimenez, C., Radenz, M.,
933 Tiesseire, A., Floutsi, A., Haarig, M., Foth, A., Chudnovsky, A., Engelmann, R.,
934 Zamorano, F., Bühl, J., and Wandinger, U.: Smoke of extreme Australian bushfires
935 observed in the stratosphere over Punta Arenas, Chile, in January 2020: optical
936 thickness, lidar ratios, and depolarization ratios at 355 and 532nm, *Atmos.*
937 *Chem. Phys.*, 20, 8003–8015, <https://doi.org/10.5194/acp-20-8003-2020>, 2020.
- 938 Pardini, F., Burton, M., Arzilli, F., La Spina, G., and Polacci, M.: SO₂ emissions, plume
939 heights and magmatic processes inferred from satellite data: The 2015 Calbuco
940 eruptions, *J. Volcanol. Geotherm. Res.* 361, 12-24, 2018.
- 941 Peterson, D. A., Fromm, M. D., McRae, R. H. D., Campbell, J. R., Hyer, E. J., Taha, G.,
942 Camacho, C. P., Kablick, G. P., Schmidt, C. C., and DeLand, M. T.: Australia's
943 Black Summer pyrocumulonimbus super outbreak reveals potential for
944 increasingly extreme stratospheric smoke events, *Npj Clim. Atmos. Sci.*, 4, 38
945 <https://doi.org/10.1038/s41612-021-00192-9>, 2021.
- 946 Peterson, D. A., Berman, M. T., Fromm, M. D., Servranckx, R., Julstrom, W. J., Hyer, E. J.,
947 Campbell, J. R., McHardy, T. M., and Lambert, A.: Worldwide inventory reveals
948 the frequency and variability of pyrocumulonimbus and stratospheric smoke
949 plumes during 2013–2023, *Npj Clim. Atmos. Sci.*, 8, 325,
950 <https://doi.org/10.1038/s41612-025-01188-5>, 2025.

- 951 Ploeger, F., Diallo, M., Charlesworth, E., Konopka, P., Legras, B., Laube, J.C., Gross, J.-U.,
 952 Günther, G., Engel, A., and Riese, M.: The stratospheric Brewer–Dobson
 953 circulation inferred from age of air in the ERA5 reanalysis, *Atmos. Chem. Phys.*,
 954 21, 8393–8412, <https://doi.org/10.5194/acp-21-8393-2021>, 2021.
- 955 Prata, A. T., Young, S. A., Siems, S. T., and Manton, M. J.: Lidar ratios of stratospheric
 956 volcanic ash and sulfate aerosols retrieved from CALIOP measurements, *Atmos.*
 957 *Chem. Phys.*, 17, 8599–8618, <https://doi.org/10.5194/acp-17-8599-2017>, 2017.
- 958 Rieger, L.A., Bourassa, A.E., and Degenstein, D.A.: Merging the OSIRIS and SAGE II
 959 stratospheric aerosol records, *J. Geophys. Res. Atmos.*, 120, 8890–8904,
 960 doi:10.1002/2015JD023133, 2015.
- 961 Sandvik, O. S., Friberg, J., Sporre, M. K., and Martinsson, B. G.: Methodology to obtain
 962 highly resolved SO₂ vertical profiles for representation of volcanic emissions in
 963 climate models, *Atmos. Meas. Tech.*, 14, 7153–7165,
 964 <https://doi.org/10.5194/amt-14-7153-2021>, 2021.
- 965 Sato, M., Hansen, J.E., McCormick, M.P., and Pollack J.B.: Stratospheric aerosol optical
 966 depths, 1850–1990, *J. Geophys. Res.* 98, 22987–22994, 1993.
- 967 Schmidt, A., Mills, M. J., Ghan, S., Gregory, J. M., Allan, R. P., Andrews, T., Bardeen, C. G.,
 968 Conley, A., Forster, P. M., Gettelman, A., Portmann, R. W., Solomon, S., and Toon,
 969 O. B.: Volcanic radiative forcing from 1979 to 2015, *J. Geophys. Res.-Atmos.*, 123,
 970 12491–12508, <https://doi.org/10.1029/2018JD028776>, 2018.
- 971 Seabrook, S., Mackay, K., Watson, S. J., Clare, M. A., Hunt, J. E., Yeo, I. A., Lane, E. M.,
 972 Clark, M. R., Wysoczanski, R., Rowden, A.A., Kula, T., Hoffmann, L.J., Armstrong,
 973 E., and Williams, M. J. M.: Volcaniclastic density currents explain widespread
 974 and diverse seafloor impacts of the 2022 Hunga Volcano eruption, *Nat.*
 975 *Commun.*, 14, 7881, <https://doi.org/10.1038/s41467-023-43607-2>, 2023.
- 976 Sheng, J.-X., Weisenstein, D.K., Luo, B.-P., Rozanov, E., Stenke, A., Anet, J., Bingemer, H.,
 977 and Peter, T.: Global atmospheric sulfur budget under volcanically quiescent
 978 conditions: Aerosol-chemistry-climate model predictions and validation, *J.*
 979 *Geophys. Res. Atmos.*, 120, 256–276, doi:10.1002/2014JD021985, 2015.
- 980 Solomon, S., Daniel, J. S., Neely, R. R., Vernier, J.-P., Dutton, E. G., and Thomason, L. W.:
 981 The persistently variable “background” stratospheric aerosol layer and global
 982 climate change, *Science*, 333, 866–870, 2011.
- 983 Surano, Jousset, P., Pallister, J., Boichu, M., Boungiorno, M.F., Budisantoso, A., Costa, F.,
 984 Andreastuti, S., Prata, F., Schneider, D., Clarisse, L., Humaida, H., Sumarti, S.,
 985 Bignami, C., Griswold, J., Carn, S., Oppenheimer C., and Lavigne F.: The 2010
 986 explosive eruption of Java's Merapi volcano—A ‘100-year’ event, *J. Volcanol.*
 987 *Geotherm. Res.* 241–242, 121–135, 2012.
- 988 Taylor, I. A., Grainger, R. G., Prata, A. T., Proud, S. R., Mather, T. A., and Pyle, D. M.: A
 989 satellite chronology of plumes from the April 2021 eruption of La Soufrière, St

- 990 Vincent, Atmos. Chem. Phys., 23, 15209–15234, [https://doi.org/10.5194/acp-23-](https://doi.org/10.5194/acp-23-15209-2023)
991 15209 2023, 2023.
- 992 Thomas, H.E., Watson, I.M., Carn, S.A., Prata, A.J., and Realmuta, V.J.: A comparison of
993 AIRS, MODIS and OMI sulphur dioxide retrievals in volcanic clouds, Geomatics,
994 Natural Hazards and Risk, 2, 217-232, 2011.
- 995 Thomason, L.W., Ernest, N., Millán, L., Rieger, L., Bourassa, A., Vernier, J.-P., Manney, G.,
996 Luo, B., Arfeuille, F., and Peter, T.: A global space-based stratospheric aerosol
997 climatology: 1979-2016, Earth Syst. Sci. Data, 10, 469–492,
998 <https://doi.org/10.5194/essd-10-469-2018>, 2018.
- 999 Vernier, J.-P., Pommereau, J.P., Garnier, A., Pelon, J., Larsen, N., Nielsen, J.,
1000 Christiansen, T., Cairo, F., Thomason, L.W., Leblanc, T., and McDermid, I.S.:
1001 Tropical stratospheric aerosol layer from CALIPSO lidar observations, J.
1002 Geophys. Res., 114, D00H10, doi:10.1029/2009JD011946, 2009.
- 1003 Vernier, J.-P., Farlie, T.D., Murray, J.J., Tupper, A., Trepte, C., Winker, D., Pelon, J., Garnier,
1004 A., Jumelet, J., Pavolonis, M., Omar, A.H., and Powell, K.A.: An Advanced System
1005 to Monitor the 3D Structure of Diffuse Volcanic Ash Clouds J. Appl. Meteorol.
1006 Clim. 10, 2125-2138, 2013.
- 1007 Vernier, J.-P., Farlie, T.D., Natarajan, M., Wiengold, F.G., Bian, J., Martinsson, B.G.,
1008 Crumeyrolle, S., Thomason, L.W., and Bedka, K.M.: Increase in upper
1009 tropospheric and lower stratospheric aerosol levels and its potential connection
1010 with Asian pollution, J. Geophys. Res., 120, doi:10.1002/2014JD022372, 2015.
- 1011 Weisenstein, D.K., Yue, G.K., Ko, M.K.W., Sze, N.-D., Rodriguez, J.M., and Scott, C.J.: A
1012 two-dimensional model of sulfur species and aerosol, J. Geophys. Res. 102,
1013 13019-13035, 1997.
- 1014 Winker, D. M., Hunt, W. H., and McGill, M. J.: Initial performance assessment of CALIOP,
1015 Geophys. Res. Lett., 34, 1–5, <https://doi.org/10.1029/2007GL030135>, 2007.
- 1016 Winker, D. M., Pelon, J., Coakley, J. A., Ackerman, S. A., Charlson, R. J., Colarco, P. R.,
1017 Flamant, P., Fu, Q., Hoff, R. M., Kittaka, C., Kubar, T. L., Le Treut, H., McCormick,
1018 M. P., Mégie, G., Poole, L., Powell, K., Trepte, K., Vaughan, M. A., and Wielicki, B.
1019 A.: The CALIPSO mission—A global 3D view of aerosols and clouds, B. Am.
1020 Meteorol. Soc., 91, 1211–1229, <https://doi.org/10.1175/2010BAMS3009.1>, 2010.
- 1021 *Data availability.* The data used are publicly available: CALIOP V4.51 lidar data
1022 (<https://search.earthdata.nasa.gov/search?fp=CALIPSO>).
- 1023 *Author contributions.* BGM planned the study, undertook most of the data analysis and
1024 wrote the paper. JF participated in the planning of the study, undertook part of the data
1025 analysis and MKS contributed. JF and MKS undertook data extraction and handling for
1026 the data analysis. All authors participated in discussions and commented on the
1027 manuscript.

1028 *Disclaimer.* The contact author and the co-authors declare that they have no competing
1029 interests.

1030 *Acknowledgements.* Aerosol products from the CALIOP sensor were produced by NASA
1031 Langley Research Center.

1032 *Financial support.* The Swedish National Space Agency, contracts 2025-00200 and
1033 2022-00157, Johan Friberg. The Crafoord Foundation, contract 20240901, Johan Friberg.
1034 [Formas, contract 2025-01869, Johan Friberg.](#) Formas, contract 2020-00997, Moa
1035 Sporre. The Swedish Research Council 2022-02836, Moa Sporre.